Structural Insights and Advanced Spectroscopic Characterization of Thiazolothiazoles: Unveiling Potential for Optoelectronic and Sensing Applications

Karolina Gutmańska,*[a] Agnieszka Podborska,[b] Andrzej Sławek,[b] Ramesh Sivasamy,[b] Lulu Alluhaibi,[c] Alexey Maximenko,[c] Anna Ordyszewska,[a] Konrad Szaciłowski,*[b, d] Anna Dołęga,[a] and Tomasz Mazur*[b]

Thiazolothiazoles (TzTzs) are planar, π-conjugated heterocyclic compounds exhibiting unique structural and optoelectronic properties. In this study, a series of symmetrically substituted thiazolothiazole (TzTz) derivatives including imidazolyl, o-vanillyl, p-vanillyl, phenyl, thiazolyl, cinnamoyl, and trifluoromethylphenyl were synthesized and extensively characterized using X-ray crystallography (XRD), Fourier-transformed infrared (FTIR), nuclear magnetic resonance (NMR), and ultraviolet-visible (UV-Vis) spectroscopies, photoluminescence, X-ray absorption near edge structure (XANES, S K-edge), and density functional calculations. The compounds demonstrated diverse intermolecular interactions, including $\pi\cdots\pi$ stacking and chalcogen bonding, which directly influenced their optical properties and electronic band structures. Several derivatives displayed promising features such as large Stokes shifts over 0.4 eV in solution and up to 1 eV in solid state and reversible resistive switching behavior, positioning them as attractive candidates for use in optoelectronic devices and emerging memristive technologies.

1. Introduction

In recent years, there has been a significant increase in interest in the study of modern organic materials with exceptional optical and electronic properties,[1] which have the potential for wide application in advanced technologies such as optoelectronics,[2] photovoltaics,[3] and biosensing.[4] A particularly promising class of compounds in this field are heterocyclic compounds, known for their ability to absorb and emit light, as well as their structural tunability, which enables the tailoring of their properties to specific application needs.[5]

[a] K. Gutmańska, A. Ordyszewska, A. Dołęga
Chemical Faculty, Department of Inorganic Chemistry, Gdansk University of Technology, Narutowicza 11/12, Gdańsk 80–233, Poland
E-mail: karolina.gutmanska@pg.edu.pl

[b] A. Podborska, A. Sławek, R. Sivasamy, K. Szaciłowski, T. Mazur
Academic Centre of Materials and Technology, AGH University of Krakow, al. Mickiewicza 30, Kraków 30–059, Poland
E-mail: szacilow@agh.edu.pl
        tmazur@agh.edu.pl

[c] L. Alluhaibi, A. Maximenko
National Synchrotron Radiation Centre SOLARIS, Jagiellonian University, ul. Czerwone Maki 98, Kraków 30–392, Poland

[d] K. Szaciłowski
Unconventional Computing Lab, University of the West of England, Bristol BS16 1QY, UK

One such compound of interest is thiazolo[5,4-d]thiazole, a heterocyclic structure composed of fused thiazole rings.[6] Its structure contains both sulfur and nitrogen atoms, which contribute to its unique physicochemical and optical properties, including intense fluorescence and strong ultraviolet absorption.[6a,7] Since their discovery in 1960, thiazolothiazoles (TzTzs) have attracted attention due to their unusual properties as well as synthetic accessibility[8] and even prospective medicinal applications.[9] The planarity of the TzTz core and its strong $\pi-\pi$ stacking tendency render TzTz derivatives effective semiconductors with excellent charge mobilities, making them ideal candidates for use in organic field-effect transistors (OFETs) and organic solar cells.[6a] Thiazolo[5,4-d]thiazole derivatives became important electron acceptors in donor-acceptor (D-A) π-conjugated systems due to their electron-deficient nature.[10]

The complexity of the absorption and emission mechanisms in these compounds arises from the π-electron conjugation within the ring, which enables efficient charge transfer and stabilization of excited states.[2d] The optical properties of TzTzs are highly sensitive to the presence of specific functional groups,[11] environmental changes such as solvent polarity,[10,12] the degree of protonation or deprotonation,[12c,13] and the presence of metal cations,[14] allowing for flexible tuning to meet the demands of various applications (for viologen-type compounds, see works of Li and Woodward).[15] Consequently, studies on photoluminescence and angular changes in optical dipoles in excited states are crucial for fully understanding their potential and require advanced spectroscopic analyzes. The fused bicyclic thiazolo[5,4-d]thiazole heterocycle may serve as an important example of the influence of the molecular shape on the final properties of the synthesized system.[16] Thiazolothiazole(TzTz) imposes completely planar conformation on its substituents, and

therefore it was applied as a stiff, strongly fluorescent spacer between the pirydyl rings of viologen-type redox couples[15b] or of 4,4′-bipyridine linkers in metal organic frameworks, that is, MOF-type materials.[17] Interestingly, the TzTz viologens mentioned above exhibit not only strong blue fluorescence with high quantum yields between 0.8 and 0.96, but some of the derivatives also show distinctive and reversible yellow-to-dark-blue electrochromism at low reduction potentials.[15b]

From a practical perspective, the ability to modify the TzTz ring facilitates tailoring their optical properties. Most of the optoelectronic applications of TzTzs (solar cells, OFETs, etc.) are based either on polymeric structures with TzTz moiety as one of the building blocks,[18] or asymmetric (usually of push-pull architecture) derivatives.[19] In this context, symmetrical derivatives have attracted much less attention. On the other hand, symmetrical derivatives pose much smaller synthetic obstacles and should also offer significant tenability of their electronic and optical properties. This could lead to the development of new dyes with high resistance to fading, precisely controlled emission parameters, and selectivity for specific biomolecules or metal ions, as well as n-type organic semiconductors,[20] which are much less common and less stable than their p-type counterparts. Given the increasing demand for optical materials with precisely controlled parameters, detailed studies on the properties of TzTzs, especially their optical and spectroscopic properties, may inspire the development of innovative technologies, particularly in fields such as chemical detection, advanced display technologies, and light energy storage.

Among the latest achievements in TzTz research, two applications of individual TzTz molecules stand out. The first involves excited-state intramolecular proton transfer systems, where the TzTz core acts as a proton acceptor, used in white organic light emitting diodes, achieving an external quantum efficiency (ηext) of 1.70% and Commission Internationale de L'Eclairage (CIE) coordinates of (0.29, 0.33).[21] TzTz compounds have the potential to revolutionize electronics and optoelectronics. The second involves helical structures formed by nonplanar substituents, which exhibit axial chirality, strong blue fluorescence, and a fluorescence efficiency of up to 0.40 in solution and polymer films. These features make them valuable for optoelectronic applications such as light detection and sensors.[11c]

It should be noted, however, that memristors (memory resistors) and other memristive devices are considered as workhorses of future electronic technologies. Memristive devices are considered key components for future electronic technologies. They are anticipated to play a major role in areas such as memory storage, computing, and neuromorphic systems. Most of the memristors reported so far are based either on oxide materials[22] or 2D chalcogenides[23] which are not compatible with microelectronic fabrication technologies. An alternative approach, compatible with spin coating and other liquid-phase processing technologies utilizes lead halide perovskites, which, along with the high toxicity of lead, pose significant stability issues.[24] TzTz have already filled a significant niche as materials for organic field effect transistors,[20,25] optoelectronic devices[6d] and photovoltaic applications.[26] However, their applicability in memristive devices has not been recognized so far; however, other organic
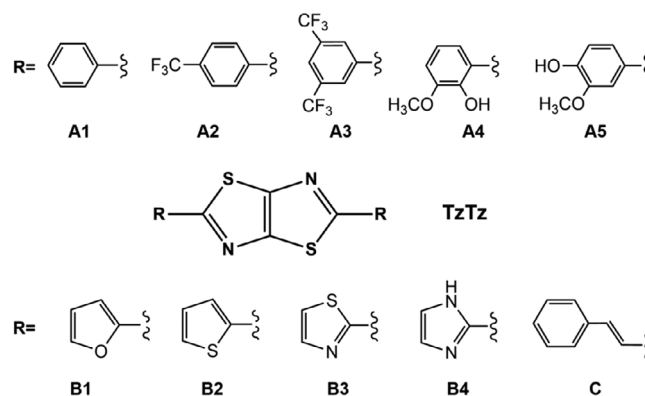
Scheme 1. Chemical structures of **TzTzs** under study.

materials of lower stability and synthetically more demanding have been suggested for this application.[27]

In this work we report structural, spectroscopic, and electronic properties of a series of TzTzs with simple aromatic substituents as well as several diphenyl derivatives substituted with electron-withdrawing (trifluoromethyl) and electron-donating (hydroxyl, methoxyl) substituents. Some of them (o-vanilin, 2-imidazoyl, and 2-thiazoyl derivatives) are also potential ligands for transition metal ions. Here we will mostly focus on structure - property relationships in the context of applications in optoelectronics, especially in memristive devices. The weak electron acceptor character of the core thiazolothiazoyl unit suggests the possibility of reversible resistive switching due to redox-controlled delocalization of electrons in molecular materials.[28]

2. Results and Discussion

2.1. Synthesis and Molecular Structure of TzTzs

The synthesis of TzTzs, including both known compounds and several new species, was carried out using the classical Hantzsch reaction.[29] In this case, the reaction involves the condensation of dithiooxamide with an appropriate aldehyde.[8a,30] This method is relatively straightforward but requires high-boiling solvents and poses challenges in isolating and crystallizing pure products. The reaction is conducted at temperatures ranging from 120 °C to 150 °C for 3–8 hours. The formation of the TzTz ring system is quite easily confirmed by the photoluminescence observable under UV light. Gradual cooling of the reaction mixture to room temperature promotes the precipitation of crystalline product, facilitating characterization and subsequent purification. Immediate purification is recommended due to the very low solubility of the final compound in common solvents.

The TzTzs studied in this work were categorized into three groups based on the different substituents at the TzTz unit: Type A, Type B, and Type C, as shown in Scheme I. Type A consists of diverse phenyl groups with electron-withdrawing and electron-donating substituents. Type B includes 5-membered heterocycles as substituents. Finally, Type C, represented by
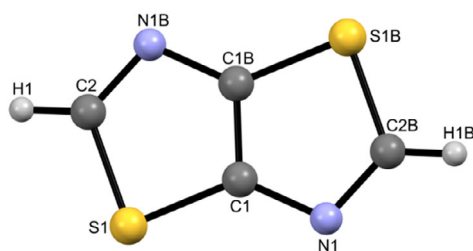
Chemistry–A European Journal

Research Article
doi.org/10.1002/chem.202501664

Chemistry Europe
European Chemical
Societies Publishing

Figure 1. Molecular structure of thiazolo(5,4-d)thiazole.[32]

Figure 3. π-stacking interactions in the crystal packing of thiazolo(5,4-d)thiazole derivatives: a) vertical; b) shifted. The longer bar represents the central TzTz unit, while the shorter bars indicate the substituents attached to the central unit.

a cinnamyl-substituted TzTz, can be summarized as a highly conjugated species.

The characterization of TzTzs should always include a detailed description of their crystal structure or, at a minimum, the identification of a phase using powder X-ray diffraction. It has been observed multiple times that crystal packing significantly influences the physical properties of these materials. Therefore, obtaining a compound in a defined polymorphic form is essential to ensure the reproducibility of its properties, particularly its luminescence.[31]

Typically, simple TzTz derivatives are flat, aromatic molecules. They adopt an anti-conformation of the nitrogen and sulfur atoms around the central double bond within the TzTz rings, along with an all-trans arrangement of their substituents. The crystal structure of the parent thiazolo(5,4-d)thiazole was first reported in 1987 by Bolognesi et al.[32] As illustrated in Figure 1, the fused thiazole rings are symmetrically arranged around an inversion center located at the midpoint of the C1—C1B bond (as designated in Bolognesi's original work). These rings are nearly perfectly coplanar, showing a maximum displacement of only 0.002 Å—a distinguishing characteristic of all derivatives of the simplest TzTz molecule.

Similar to the aromatic hydrocarbons, the crystal packing of aromatic TzTzs may be categorized into the typical patterns such as herringbone or parallel illustrated in Figure 2a, b.[33] In the case of larger TzTz molecules or less usual intermolecular interactions, the grid arrangement of molecules is possible shown in Figure 2c (for example, see the crystal structure of 2,5-bis(2-fluorophenyl)[1,3]thiazolo[5,4-d][1,3]thiazole).[34] We distinguish this grid type to emphasize the interactions between the long edge of one molecule and the aromatic system or heteroatoms of the other molecule, for example, CH···π interactions in 2,5-bis(pyridin-4-yl)[1,3]thiazolo[5,4-d][1,3]thiazole.[31b] On the other hand, the π-stacking interactions in the crystals of
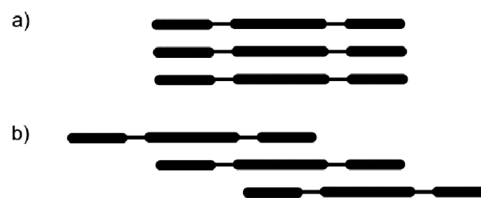
TzTzs may be realized in the form of approximately vertical or shifted stacks (Figure 3).

The crystal data for the new structures of **A3**–**A5**, **B1**, **B4**, and, **C** are presented in Table S1 of the Supplementary Materials. The geometrical parameters of the molecules, including bond lengths and angles, are summarized in Tables S2, S3. Selected intermolecular interactions are listed in Tables 1, 2. Corresponding data for the remaining compounds can be found in the following references: **A1**, [293 K, yellow,[35] 100 K, colorless[36]] **A2**,[37] **B2**,[38] and **B3**.[39]

The molecular architectures of all TzTzs depicted in Figure 4 exhibit a characteristic coplanar arrangement of flat aromatic systems. Even in compound **C**, which uniquely includes an additional linker between its aromatic rings, this coplanarity is maintained. Consistently, the molecules are centrosymmetric, as previously discussed in this chapter, with an inversion center positioned at the midpoint of the C—C bond within the TzTz core. In compounds **A4**, **A5**, and **B1**–**B3**, this inherent centrosymmetry dictates a *trans* configuration for the asymmetrically substituted phenyl rings or heterocycles. In **A4**, the conformation observed through diffraction measurements is stabilized by an intramolecular hydrogen bond, O1—H1···N1. While the geometrical parameters of molecules, which are collected in Table S2, do not vary significantly between the compounds, the principal distinctions among all these compounds emerge upon examining their crystal packing arrangements, necessitating a separate analysis for each structure type. The statement is further supported by the analysis of the radial distribution of sulfur-sulfur pairs, which serves as a reliable measure of crystal packing in the case of TzTzs and highlights significant differences among the compounds (Figure S1). We focused on the sulfur-sulfur distance distribution to support our analysis of sulfur K-edge X-ray absorption spectroscopy (XAS) for the studied TzTzs.
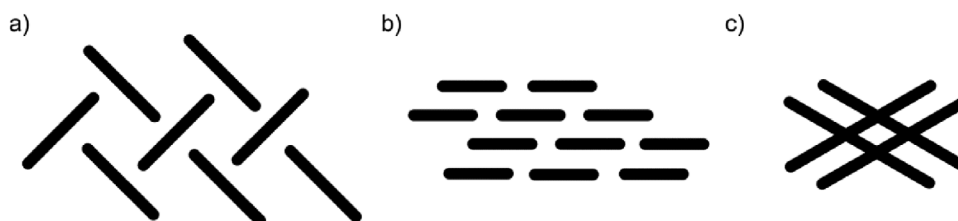
Figure 2. Typical crystal packing of thiazolo(5,4-d)thiazole derivatives: a) herringbone; b) parallel; c) grid. More than one 2D pattern may be observed in various directions.[33]

Chemistry–A European Journal

Research Article
doi.org/10.1002/chem.202501664

Chemistry Europe
European Chemical
Societies Publishing
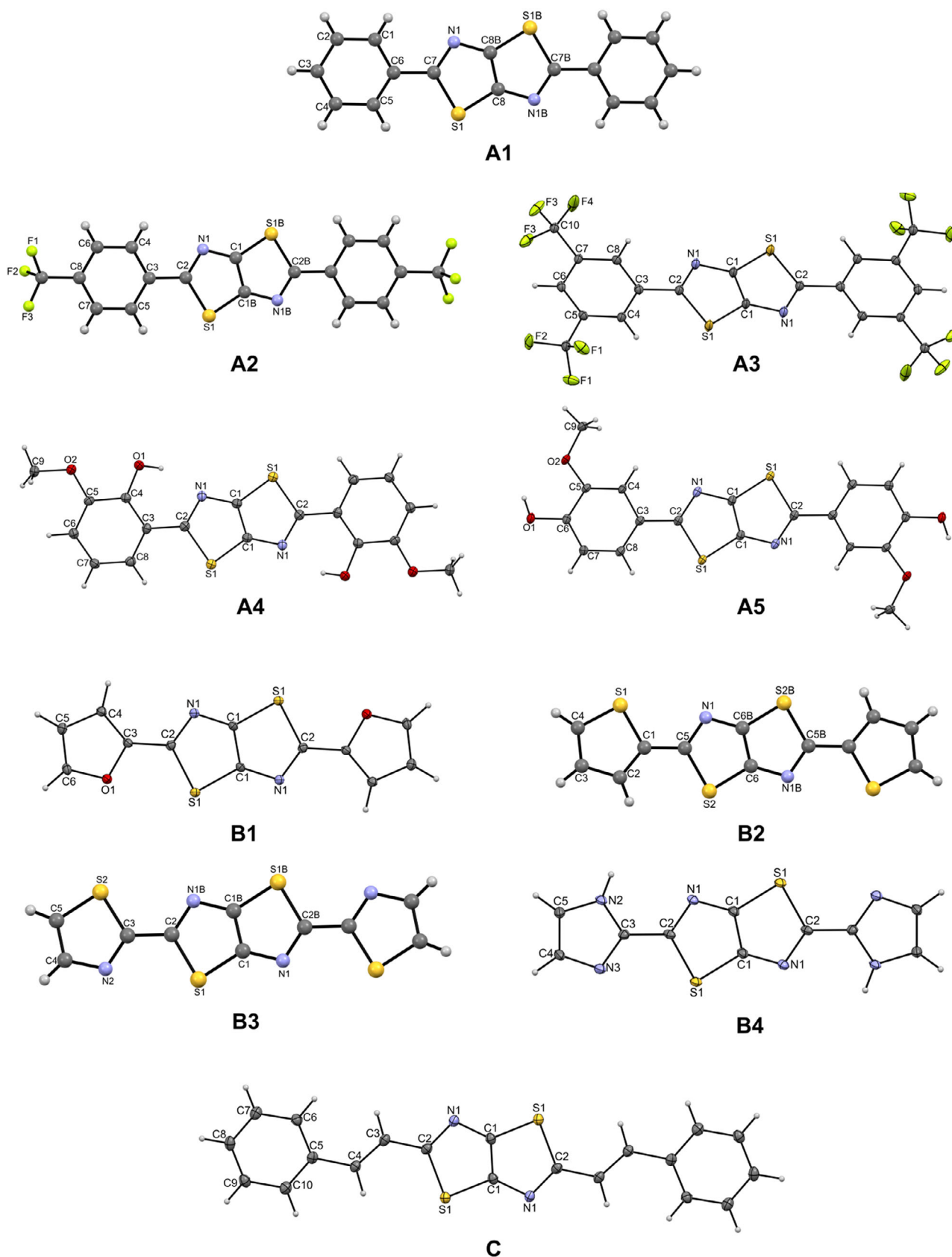
Figure 4. Molecular structures of **A1–A5**, **B1–B4**, and **C**, with the numbering schemes. The structures determined in this work (**A3–A5**, **B1**, **B4**, **C**) are depicted with 50% probability ellipsoids, while the remaining structures, sourced from the literature, are presented as ball-and-stick models. The source data for these figures were obtained from the Cambridge Structural Database (CSD).

Chemistry–A European Journal

Research Article
doi.org/10.1002/chem.202501664

Chemistry Europe
European Chemical
Societies Publishing

Table 1. Chalcogen and chalcogen-pnictogen interactions in the studied compounds.

Compound	A1a	A1b	A2	A3	A4	A5	B1	B2	B3	B4	C
S1/S2···S1$^{iii/iv/vi}$/S1B$^{i/ii}$S2B^{v} [Å]	3.566	3.532	-	-	3.775	3.964	-	3.579	3.507	3.744	3.360
S1···N1^{vii} [Å]	-	-	-	-	-	-	3.343	-	-	-	-

Note: ^{i}:1-x,2-y,2-z; ^{ii}:2-x,2-y,1-z; ^{iii}:1-x,-y,-z; ^{iv}:x,1+y,z; ^{v}:-x,1-y,-z; ^{vi}:1+x,y,z; ^{vii}:-x,2-y,1-z; ^{viii}:x,-1+y,z, ^{ix}:1/2-x,-1/2+y,1.5-z.

Figure 5. Crystal packing of **B1**: a) along axis b, the shortest intermolecular contacts include two CH···O interactions and one CH···π; b) along axis a, the shortest π···π stacking interactions are shown; c) along a, the shortest contact between sulfur and nitrogen atoms is visualized.

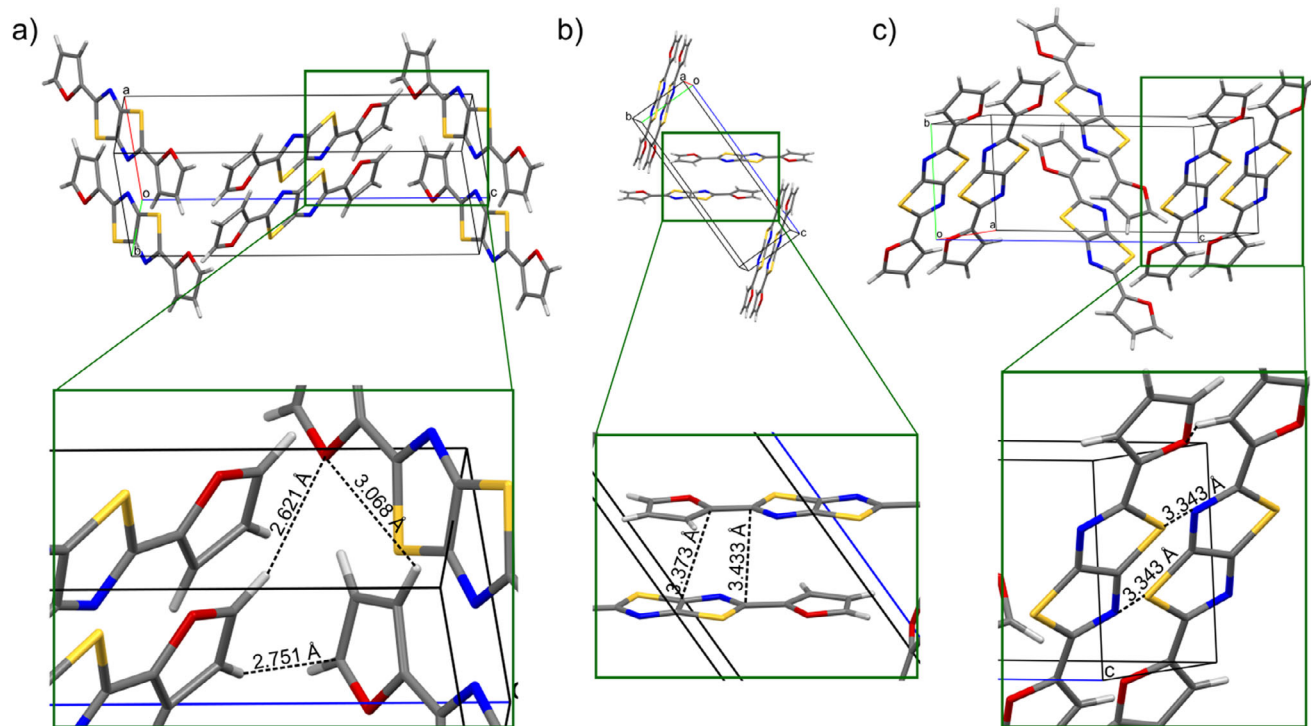Among the studied TzTzs, there are 6 typical herringbone packings: **A1**, **A4**, **B1**-**B3**, and **C**; only one parallel, **A3**; and three examples of grid: **A2**, **A5**, and **B4**.

The compounds **A1** and **B1**-**B3** realize very similar type of intermolecular interactions, which involve CH···π, CH···heteroatom, chalcogen···chalcogen or chalcogen···pnictogen, and shifted π···π stacking interactions shown in Figure 5 for **B1**. Tables 1, 2 characterize some of these intermolecular contacts for all TzTzs.

The only example of parallel packing among the studied compounds, **A3**, crystallizes in the orthorhombic system with the space group *Ibam*, in contrast to the remaining compounds, which crystallize in the monoclinic crystal system (Table S1). The centrosymmetric molecule is planar, except for the fluorine atoms in the trifluoromethyl groups. The molecules form layers along the *a* and *b* axes, which, stack along the *c* axis. Within each layer, the molecules of compound **A3** are stabilized by C—H···F hydrogen bonds which also contribute to interlayer stabilization.

Furthermore, the presence of as many as 12 fluorine atoms per molecule facilitates the formation of interlayer halogen interactions, which play a key role in layer stabilization. The torsion angle θ for C—F···F—C, defined in Figure 6a, is 162.86°, and the fluorine-fluorine distance is 2.826 Å—typical values for the first type of F···F interactions in organic compounds.[40] The crystal lattice is further stabilized by vertical π···π stacking interactions as defined in Figure 3b and illustrated in Figure 6b. Interestingly, the parallel-aligned molecules exhibit a slight rotation, leading to variations in π···π stacking interaction lengths (Figure 6c). The closest interactions occur between the TzTz systems of neighboring molecules, while the more distant ones are observed between the 3,5-trifluoromethylphenyl substituents. The shortest distances shown in Figure 6b are as follows: between the centroids of C1—C1^{i}··· C1^{ii}—C1^{iii} bonds – 3.718 Å, and C6(phenyl ring)···C7^{ii}(phenyl ring)—3.822 Å (^{i}:1-x,1-y, z; ^{ii}:1-x, y, 1/2-z; ^{iii}:x,1-y, 1/2-z).

The typical S···S or S···N interactions commonly observed in thiazole systems are absent in this structure. These interactions were present in all previously studied compounds and played a significant role in stabilization. The absence of S···S/N interactions, combined with the presence of halogen interactions, highlights how substituent modifications influence the stabilization mechanisms.

Table 2. Shortest $\pi\cdots\pi$ stacking interactions in the studied compounds characterized by the distances between the centroids of the rings, slippage angle and slippage value.

| Compound	π-π Stacking Interactions	Distances Between Cg-Cg [Å]	Slippage Angle [°]/ Slippage Value [Å]	Cg Definition
A1a	$Cg_{Ph1}\cdots Cg_{TzTz1}$	3.787	16.17/1.329	Cg_{Ph1}: C1–C2–C3–C4–C5–C6 Cg_{TzTz1}: S1^i–C7^i–N1^i–C8B^i–C8^i
	$Cg_{TzTz2}\cdots Cg_{TzTz3}$	4.005	19.92/1.699	Cg_{TzTz2}: S1–C7–N1–C8B^{iii}–C8 Cg_{TzTz3}: S1^{ii}–C7^{ii}–N1^{ii}–C8B^{ii}–C8^i
A1b	$Cg_{Ph2}\cdots Cg_{TzTz4}$	3.715	16.65/1.337	Cg_{Ph2}: C3–C4–C5–C6–C7–C8 Cg_{TzTz4}: C1B^{iv}–C1^i–N1^i–C2^i–S1B^{iv}
	$Cg_{TzTz5}\cdots Cg_{TzTz6}$	3.935	19.86/1.662	Cg_{TzTz5}: C1B^v – C1– N1– C2– S1B^v Cg_{TzTz6}: C1B^{iv}–C1^i–N1B^{iv}–C2B^{iv}–S1^i
A2	$Cg_{Ph3}\cdots Cg_{TzTz7}$	3.766	15.32/1.242	Cg_{Ph3}: C3^{vi}–C4^{vi}–C5^{vi}–C6^{iv}–C7^{vi}–C8^{vi} Cg_{TzTz7}: C1–C1B^{vii}–N1B^{vii}–C2B^{vii}–S1B^{vii}
	$Cg_{Ph3}\cdots Cg_{TzTz8}$	3.949	20.72/1.716	Cg_{Ph3}: C3^{vi}–C4^{vi}–C5^{vi}–C6^{iv}–C7^{vi}–C8^{vi} Cg_{TzTz8}: C1B^{vii}–C1–N1B–C2–S1
A3	$Cg_{TzTz9}\cdots Cg_{TzTz10}$	3.764	8.93/0.584	Cg_{TzTz9}: C1^{ix}–C1–N1–C2–S1^{ix} Cg_{TzTz10}: C1^{xi}–C1^x–N1^x–C2^x–S1^{xi}
	$Cg_{Ph4}\cdots Cg_{Ph5}$	4.058	23.56/1.621	Cg_{Ph4}: C3–C4–C5–C6–C7–C8 Cg_{Ph5}: C3^{viii}–C4^{viii}–C5^{viii}–C6^{viii}–C7^{viii}–C8^{viii}
A4	$Cg_{TzTz12}\cdots Cg_{Ph6}$	3.642	12.07/1.050	Cg_{TzTz12}: C1– C1^{xii} – N1^{xii} – C2^{xii} – S1^{xii} Cg_{Ph6}: C3^{xiii}–C4^{xiii}–C5^{xiii}–C6^{xiii}–C7^{xiii}–C8^{xiii}
	$Cg_{TzTz11}\cdots Cg_{Ph6}$	3.659	12.70/1.107	Cg_{TzTz11}: C1^{xii}–C1–N1–C2–S1 Cg_{Ph6}: C3^{xiii}–C4^{xiii}–C5^{xiii}–C6^{xiii}–C7^{xiii}–C8^{xiii}
A5	$Cg_{Ph7}\cdots Cg_{Ph8}$	3.964	20.09/1.776	Cg_{Ph7}: C3–C4–C5–C6–C7–C8 Cg_{Ph8}: C3^{xiii}–C4^{xiii}–C5^{xiii}–C6^{xiii}–C7^{xiii}–C8^{xiii}
	$Cg_{TzTz13}\cdots Cg_{TzTz14}$			Cg_{TzTz13}: C1–C1–N1–C2–S1^{xiv} Cg_{TzTz14}: C1^{xv}–C1^{xv}–N1^{xv}–C2^{xv}–S1^{xiv}
B1	$Cg_{Fh1}\cdots Cg_{TzTz16}$	3.537	12.91/0.942	Cg_{Fh1}: C3^{iv}–C2^{iv}–C1^{iv}–S1^{iv}–C4^{iv} Cg_{TzTz16}: C1–C1^v–N1^v–C2^v–S1
	$Cg_{Fh1}\cdots Cg_{TzTz15}$	3.584	15.14/1.112	Cg_{Fh1}: C3^{iv}–C2^{iv}–C1^{iv}–S1^{iv}–C4^{iv} Cg_{TzTz15}: C1^v–C1–N1–C2–S1^v
B2	$Cg_{TzTz17}\cdots Cg_{Th1}$	3.981	21.40/1.628	Cg_{Th1}: C3^{xx}–C2^{xx}–C1^{xx}–S1^{xx}–C4^{xx} Cg_{TzTz17}: C6B^{xvi}–C6–N1–C5–S2
B3	$Cg_{Tz1}\cdots Cg_{TzTz18}$	3.595	10.41/0.766	Cg_{Tz1}: C4^i–C5^i –N2^i –C3^i–S1^i Cg_{TzTz18}: C1–S1–C2–N1B^{xx}–C1B^{xx}
	$Cg_{Tz1}\cdots Cg_{TzTz19}$	3.717	16.15/1.224	Cg_{Tz1}: C4^i–C5^i –N2^i –C3^i–S1^i Cg_{TzTz19}: C1B^{xx}–S1B^{xx}–C2B^{xx}–N1–C1
B4	$Cg_{TzTz20}\cdots Cg_{TzTz21}$	3.540	10.07/0.861	Cg_{TzTz20}: C1^{xvii}–C1^{xix}–N1^{xix}–C2^{xix}–S1^{xvii} Cg_{TzTz21}: C1–C1–N1–C2^{iv}–S1^{iv}
	$Cg_{TzTz22}\cdots Cg_{TzTz21}$	3.744	17.14/1.494	Cg_{TzTz22}: C1^{xix} –C^{xvii} –N1^{xvii} –C2^{xvii} –S1^{xix} Cg_{TzTz21}: C1–C1–N1–C2^{iv}–S1^{iv}
	$Cg_{Im1}\cdots Cg_{Im2}$	3.744	17.14/1.534	Cg_{Im1}: N2–C3–N3–C4–C5 Cg_{Im2}: N2^{xvii}–C3^{xvii}–N3^{xvii}–C4^{xvii}–C5^{xvii}
C	$Cg1_{C=C}\cdots Cg_{TzTz25}$	3.471	1.73/0.133	$Cg1_{C=C}$: C3^{iv}–C4^{iv} Cg_{TzTz25}: C1–C1^v–N1^v–C2^v–S1
	$Cg2_{C=C}\cdots Cg_{Ph9}$	3.475	1.47/0.113	$Cg2_{C=C}$: C3^v–C4^v Cg_{Ph9}: C5^{iv}–C6^{iv}–C7^{iv}–C8^{iv}–C9^{iv}–C10^{iv}
	$Cg_{TzTz23}\cdots Cg_{TzTz24}$	3.711	15.21/1.211	Cg_{TzTz23}: C1^v–C1–N1–C2–S1^v Cg_{TzTz24}: C1^i–C1^i–N1^{iv}–C2^{iv}–S1^i

Note: Cg_{Ph} – centroid of the phenyl ring; Cg_{Tz} – centroid of the thiazole ring; Cg_{TzTz} – centroid of the thiazole ring from the TzTz system; $Cg_{C=C}$ – centroid of the C=C bond determined for the compound C; Cg_{Th} – centroid of the thiophene ring; Cg_{Im} – centroid of the imidazole ring; Cg_{Fh} - centroid of the furyl ring. Symmetry operations: ^{i}:x,-1+y,z; ^{ii}:2-x,1-y,2-z; ^{iii}:2-x,2-y,2-z; ^{iv}:1-x,1-y,1-z; ^{v}:1-x,2-y,1-z; ^{vi}:-x,-1+y,z; ^{vii}:-x,-y,-z; ^{viii}:1-x,y,1/2-z; ^{ix}:1-x,1-y,z; ^{x}:1-x,y,1/2-z; ^{xi}:x,1-y,1/2-z; ^{xii}:2-x,-y,1-z; ^{xiii}:1-x,y,1/2-z; ^{xiv}:2-x,1-y,1-z; ^{xv}:x,1+y,z; ^{xvi}:1-x,1-y,-z; ^{xvii}:-1+x,y,z; ^{xviii}:1-x,3-y,1-z; ^{xix}:-x,1-y,1-z; ^{xx}:1-x,-y,-z.

Chemistry–A European Journal

Research Article
doi.org/10.1002/chem.202501664

Chemistry
Europe
European Chemical
Societies Publishing
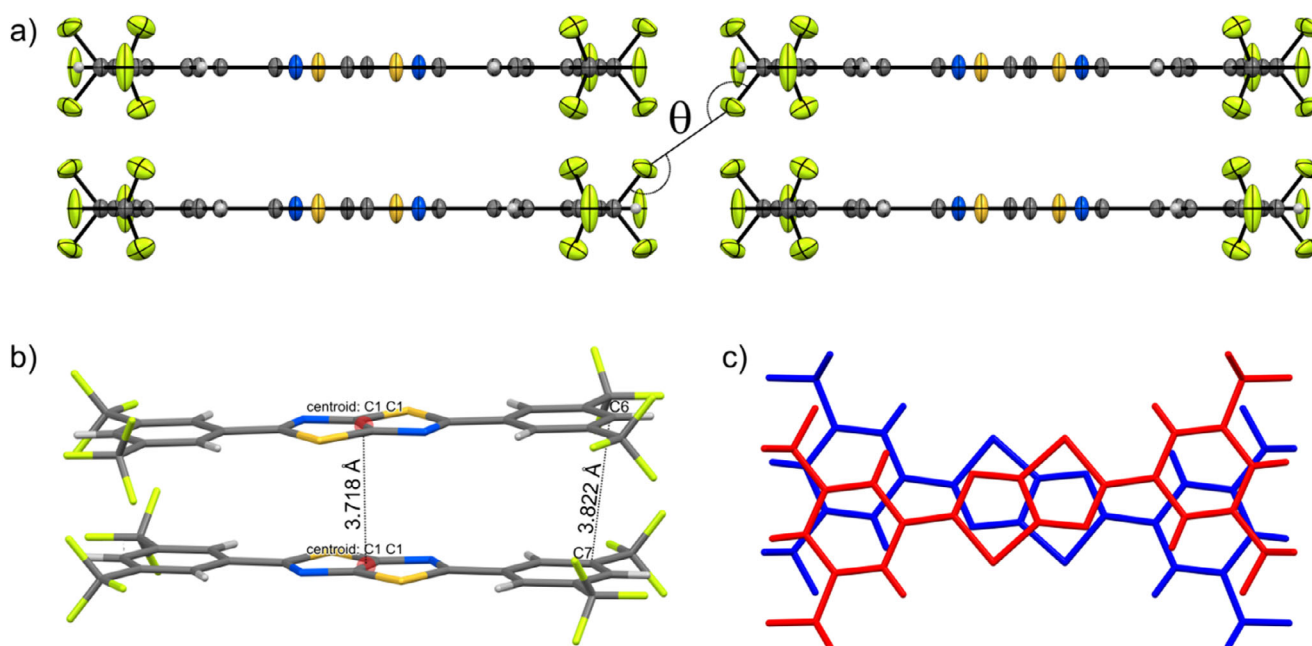
Figure 6. Crystal packing of **A3**: a) visualized along axis a, the torsion angle θ for C—F···F—C, bonds is shown; b) visualized approximately along axis a, the shortest $\pi\cdots\pi$ stacking interactions are shown; c) visualized along c to illustrate the rotation of the molecules between the layers.
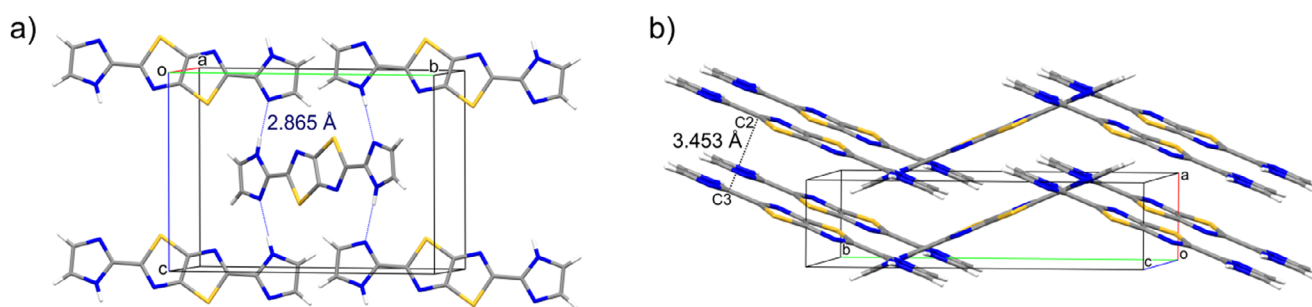
Figure 7. Crystal packing of **B4**: a) along axis a, the hydrogen bonding chains are visualized; b) along axis c, to illustrate the $\pi\cdots\pi$ stacking interactions.

The final type of crystal packing, observed in compounds **A2**, **A5**, and **B4**, is a grid arrangement, as illustrated in Figure 2c. In this arrangement, the predominant intermolecular interactions occur along the longer edge of the approximately planar molecule. In Figure 7 we provide compound **B4** as an example, where the molecular orientation is dictated by the formation of N—H···N hydrogen bonds between the imidazole substituents and the TzTz system (Figure 7a). Chains of hydrogen bonds extend along the *c*-axis, while in another direction, the crystal structure is stabilized by shifted $\pi\cdots\pi$ stacking interactions (Figure 7b).

The crystal packings of the remaining compounds **A1**, **A2**, **A4**, **A5**, **B2**, **B3**, and **C** are illustrated in Figure S2, S3 of the supplementary materials. The selected intermolecular interactions are additionally listed in Tables 1, 2 and Figure 8, which shows the contributions of various short contacts on Hirshfeld surfaces of the studied molecules. We would like to point to the interactions summarized for two molecular structures of **A1** deposited in CSD – **A1**a and **A1**b.[35,36] Though the unit cells were selected in a different way for these two measurements, the interac-

tion diagram generated with the Crystal Explorer[41] indicates the same crystal packing in both cases. Moreover, as expected, for **A1** and **C** we observe a very large percentage of hydrophobic H···H interactions, for **A2** and **A3** a very large percentage of diverse F···X contacts, for **A4**, **A5** and **B1** O···X contacts, while **B4** is distinguished by a substantial contribution of NH···N hydrogen bonds.

2.2. Electronic Properties of TzTzs

The thiazolo[5, 4-d]thiazole core is a bicyclic heterocyclic aromatic moiety with 10 π electrons, thus is isoelectronic with naphthalene and thieno[3, 2-b]thiophene. The presence of heteroatoms significantly changes their geometry as well as local and global electronic properties. All three molecules are planar, but in the case of naphthalene, introduction of any substituent generates a significant steric hindrance due to hydrogen atoms in vicinal positions. In the case of thienothiophene it is highly reduced, as there are only two hydrogen atoms at each ring.

Chem. Eur. J. **2025**, *0*, e202501664 (7 of 24)

© 2025 The Author(s). Chemistry – A European Journal published by Wiley-VCH GmbH

Chemistry–A European Journal

Research Article
doi.org/10.1002/chem.202501664

Chemistry Europe
European Chemical
Societies Publishing
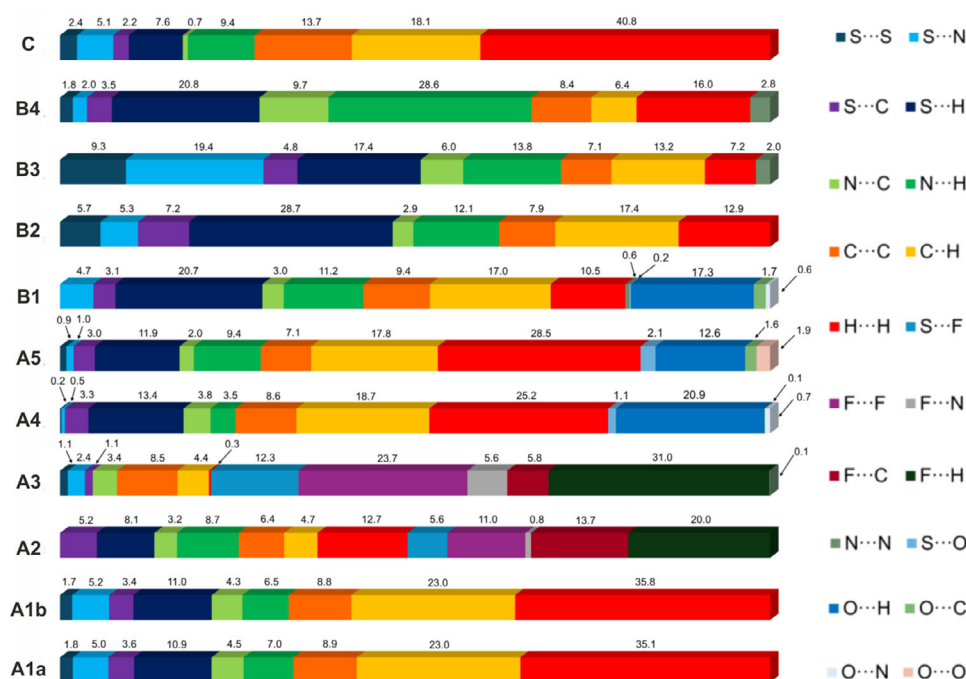
Figure 8. The contributions of various types of contacts on the Hirshfeld surfaces of the studied TzTzs. Analysis performed with the use of CrystalExplorer.[41].
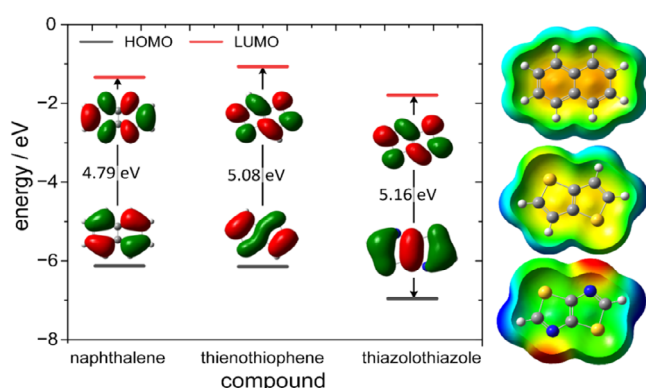
Figure 9. Energy and contours of frontier orbitals of naphthalene, thienothiophene, and TzTz along with electrostatic potentials mapped onto electron density isosurface as calculated using the DFT approach at the B3LYP/TZVP level of theory. The Electrostatic potential color scale spans from − 0.04 a.u. (red) to + 0.04 a.u. (dark blue) and is identical for all three molecules.

In the case of TzTz, no steric hindrance should be present, which may render formation of extended planar conjugated systems much easier. Globally, thienothiophene has slightly higher energies of frontier orbitals, which emphasizes its character as an electron donor. This feature of thienothiophene is exploited in the design and fabrication of high-mobility organic p-type semiconductors.[42] In contrast to thienothiophene, TzTz exhibits the characteristics of a moderate electron acceptor (Figure 9), with a LUMO level that is 0.46 eV lower compared to naphthalene. HOMO-LUMO separations increase on introduction of heteroatoms from 4.79 eV for naphthalene to 5.16 eV for TzTz.

Introduction of heteroatoms results in local changes of electron density. In the case of naphthalene, the whole ring system

bears a local negative charge due to the symmetrical delocalized cloud of π electrons. The Introduction of sulfur slightly decreases the negative charge in the π-electron cloud, which also extends to the lone electron pair at sulfur atoms. In the case of TzTz, the changes are striking: the nitrogen atoms carry the largest negative charge, while the peripheral protons are positively charged (Figure 9). This change may play a crucial role in molecular arrangement and intermolecular interactions in the solid phase.

2.3. Electron Structure
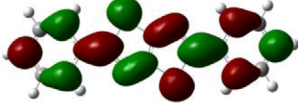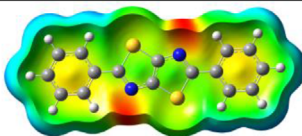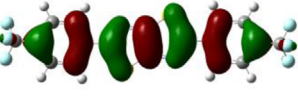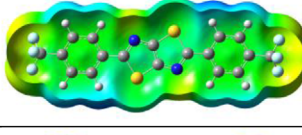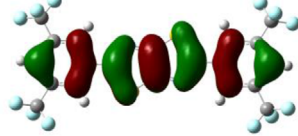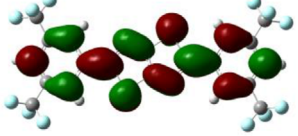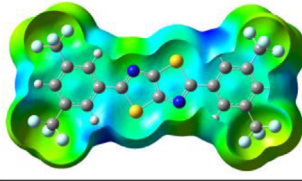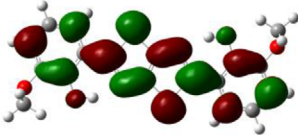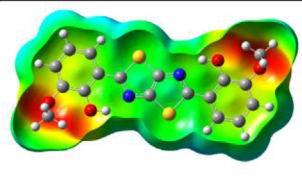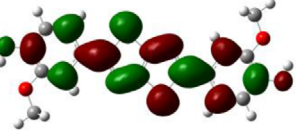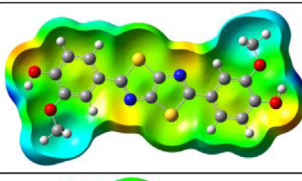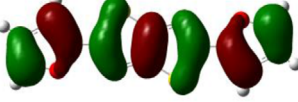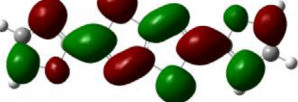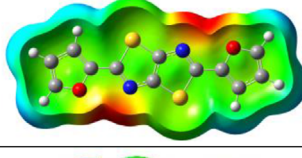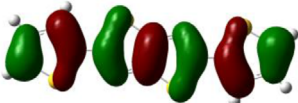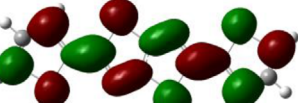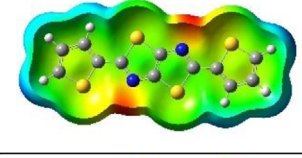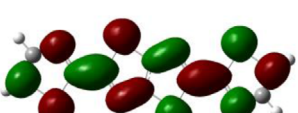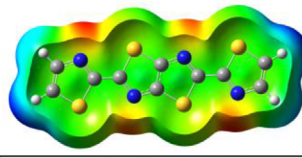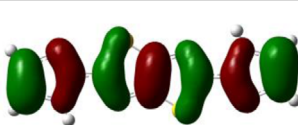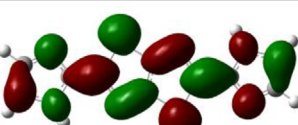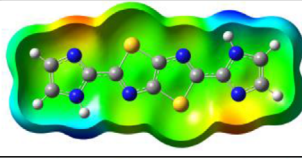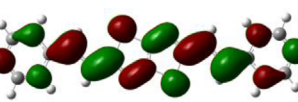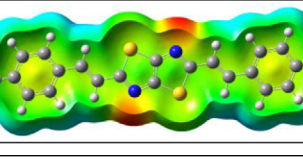
DFT geometry optimization confirms planarity of all studied molecules. As a consequence, electronic π conjugation extends over whole molecules, including aromatic or unsaturated substituents. Frontier orbital delocalization clearly indicates this process – see Table 3. Introduction of moderately electron-withdrawing substituents, like in **B3**, or electron-donating groups as in **B2** does not change charge distribution in the TzTz core.

Stronger electron acceptors, which is the case of **A2** and **A3**, or the presence of electron donors, as in **A4** and **A5** significantly change the charge distribution in the TzTz core. The strong negative character of nitrogen atoms vanishes, and the distribution of charge becomes more uniform (**A2**, **A3**, **A5**) or becomes dominated by the substituent (**A3**, **A4**). This behavior may have further consequences on transport phenomena in these materials when applied as semiconductors, as well as may affect their luminescence and other optical properties.

Along with rather minor changes in local electrostatic charge distribution, the introduction of electron donors or electron

Chemistry–A European Journal

Research Article
doi.org/10.1002/chem.202501664

Chemistry Europe
European Chemical
Societies Publishing

Table 3. Contours of frontier orbitals and maps of electrostatic potential distribution for studied TzTzs as calculated by the DFT method at the b3lyp/tzvp level of theory. The Electrostatic potential color scale spans from − 0.04 *a.u.* (red) to + 0.04 *a.u.* (dark blue) and is identical for all three molecules.

Chem. Eur. J. **2025**, *0*, e202501664 (9 of 24)

© 2025 The Author(s). Chemistry – A European Journal published by Wiley-VCH GmbH

Chemistry–A European Journal

Research Article
doi.org/10.1002/chem.202501664

Chemistry
Europe
European Chemical
Societies Publishing

Figure 10. Orbital energy diagrams (left side of the figure) and HOMO-LUMO gaps (right side of the figure) for all studied TzTzs derived from DFT calculations for single molecules at the B3LYP/TZVP level of theory. Dashed lines are reference levels for diphenyl derivative **A1**.

acceptors significantly changes energies of frontier orbitals, with the HOMO level being the most sensitive one (Figure 10a). Interestingly, just rearrangement of substituents in vanillin derivatives results in a transition from mild electron acceptor to strong electron donor. As the sensitivity of HOMO and LUMO orbitals to the substituents is different, the HOMO-LUMO energy separation also significantly changes with substituents (Figure 10b). This offers an easy tool for engineering the excited states and other photophysical properties of TzTzs, for example ability to engage in photoinduced electron transfer reactions, which may have severe consequences for their applications as fluorescent labels or homogeneous photocatalysts. It may also be important from the point of view of optoelectronic applications.

It has already been noted that various TzTz derivatives assume various special arrangements in the solid phase. It turns out that these arrangements also affect the electronic structure of solid phases. The most striking difference is observed in the case of **A2** and **A3** molecules. The first one crystallizes in parallel stacks without any shift between neighboring molecules, whereas the latter crystallizes in a herringbone structure. It was found that slipping of two adjacent TzTz molecules results in significant delocalization of π orbitals over neighboring molecules (Figure 11), whereas a perfect face-to-face arrangement prevents such interaction. It may be related to the long-distance sulfur-nitrogen attractive interaction due to a significant difference in electronegativity: 2.5 and 3.00 for sulfur and nitrogen, respectively, and their local D-A character. It is also possible that the presence of a larger number of strong electron acceptors, such as trifluoromethyl moieties in **A3** results in electron density depletion in the core. The latter effect is, however, less probable, as the local Mulliken charges of atoms are not much affected by the substituents. The HOMO contour for **A3** clearly suggests some antibonding interaction between adjacent molecules. These interactions are directly related to the transport properties of solid phases. One can assume that the principal charge transport mechanism will be electron hopping. The probability of electron transfer between neighboring molecules in solid TzTzs can be described using Marcus formalism (Equation 1):[43]

$$k_{\mathrm{et}} = \frac{2\pi}{\hbar} |H_{\mathrm{DA}}|^2 \frac{1}{\sqrt{4\pi \lambda k_{\mathrm{B}} T}} \exp\left(\frac{-(\lambda + \Delta G^o)^2}{4\pi \lambda k_{\mathrm{B}} T} \right) \qquad (1)$$
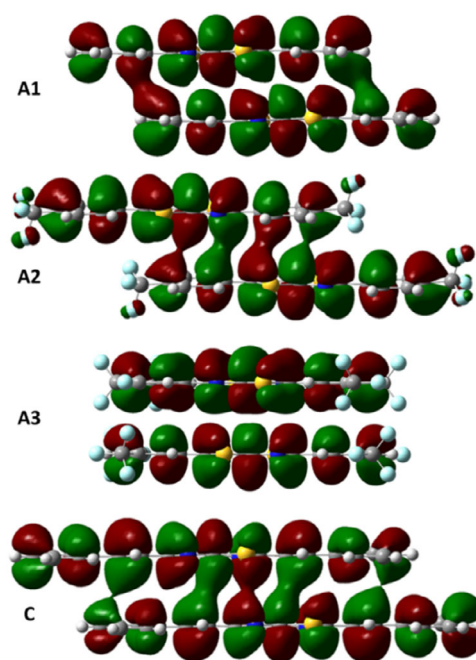
Figure 11. Frontier orbitals of molecular dimers **A1···A1**, **A2···A2**, **A3···A3,** and **C···C** as calculated for frozen, X-ray crystallography (XRD)-derived geometries, using DFT methodology at the B3LYP/TZVP level of theory.

where $|H_{\mathrm{DA}}|$ is the electronic coupling matrix element between adjacent molecules, λ is the reorganizational energy, k_{B} is the Boltzmann constant, T is the absolute temperature, and ΔG^o is the free enthalpy of the electron transfer reaction. Thus, the electronic conductivity of the molecular material is directly related to the electron transfer rate between closest neighbors in the solid.[44] In the case of molecular materials like TzTzs, where electron donor and electron acceptor are identical molecules involved in an electron exchange process, $\Delta G^o = 0$. When the process takes place in the molecular solid, the external reorganization energy, resulting from the rearrangement of the solvent molecules, can be neglected, and the internal reorganization energy should be similar for all compounds.

The electronic coupling element can be calculated based on HOMO and LUMO orbitals splitting due to the interaction of the molecule of interest with its nearest neighbor in the lattice as (Equations 2, 3):[45]

Chemistry–A European Journal

Research Article
doi.org/10.1002/chem.202501664

Chemistry Europe
European Chemical
Societies Publishing

Table 4. Electron coupling elements for electron and hole transfer for TzTz derivatives.

Compound	Neutral Dimer		Negatively Charged Dimer	
	$|H_{DA}|_{hole}$ [meV]	$|H_{DA}|_{electron}$ [meV]	$|H_{DA}|_{hole}$ [meV]	$|H_{DA}|_{electron}$ [meV]
A1	63.0	25.0	1411.6	449.3
A2	0.8	49.7	1446.0	429.1
A3	132.0	56.2	1411.3	364.8
A4	84.1	27.1	1407.9	511.8
A5	122.6	15.5	1345.9	475.0
B1	120.4	64.2	1270.1	532.5
B2	26.8	11.8	1320.6	477.0
B3	125.9	31.6	1319.8	461.2
B4	90.9	55.5	1374.4	463.1
C	16.9	41.0	1254.6	321.8

$$|H_{DA}|_{hole} = \frac{1}{2}\left(E_{HOMO} - E_{HOMO-1}\right) \qquad (2)$$

$$|H_{DA}|_{electron} = \frac{1}{2}\left(E_{LUMO+1} - E_{LUMO}\right) \qquad (3)$$

Electronic coupling elements are collected in Table 4. Quite unexpectedly, the **A3** molecule, which does not show any overlap of HOMO orbitals of individual molecules, shows the highest coupling matrix element of all studied compounds. *p*-vanilin- **A5**, furyl- **B1** and thiazoyl- **B3** derivatives are also promising candidates for higher hole mobilities. Matrix coupling elements for electron mobility are much lower, therefore, despite electron acceptor properties of TzTzs, they may show good performance as *p*-type semiconductors. This is also substantiated by electron coupling matrix elements calculated for negatively charged dimers — charging increases the probability of electron transfer by ca. 2 orders of magnitude (hole transfer) compared to a much smaller, by 1 order of magnitude, increase of electron transfer probability. This feature may not be very suitable for applications in OFETs but is essential for memristive applications.[28,46]

More information on the electronic structure of these materials is delivered by the periodic DFT calculations. The calculated crystal structure details and the calculated band gaps of the samples are listed in the Table S4-S6. The optimized geometries for all the compounds are presented in Figure S4, S5. The fully relaxed, geometry-optimized structures of the TzTz crystals were used to calculate their electronic structures that are shown in Figure 12 for **A1**, **A3**, and **A4** and Figure S6 for the rest of the compounds. Paths through the Brillouin zone for the crystal structure calculation are shown in Figure S7.

All investigated crystals exhibit the valance band maximum (VBM) near the Fermi level, which suggests a *p*-type semiconductor. The density of states shows the dense charge distribution, indicating the presence of multiple electronic states. From the projected density of states (PDOS) plots, the CBM is predominantly influenced by the electron-deficient TzTz group which behaves as an electron acceptor. In contrast,
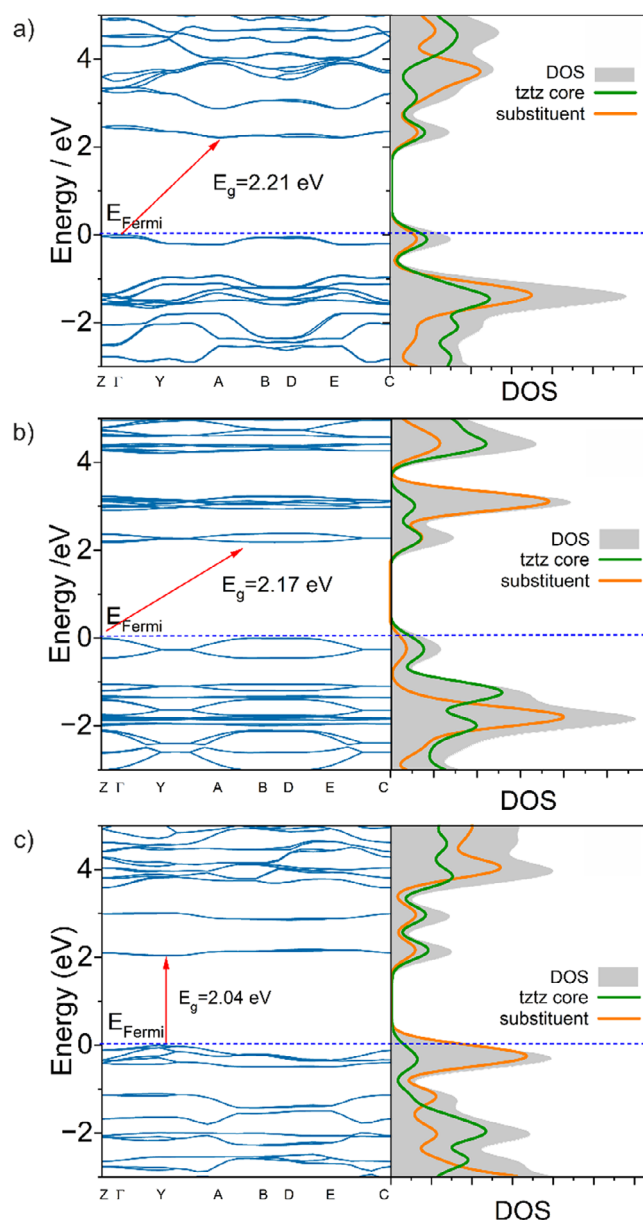
Figure 12. Theoretical band structure and partial density of states (PDOS, division between TzTz core and substituent) for the most representative TzTz derivatives: a) A1, "basic" compound with an unsubstituted phenyl ring, b) A3, electron acceptor functional groups —CF_3 and c) A4, electron donor functional group —OMe.

the VBM is dominated by the electron-rich groups: 2-thiazoyl, phenyl, phenylethenyl, trifluoromethylphenyl, 2-imidazoyl, 2-methoxyphenyl, 2-furanyl, 2-thienyl, and 3-methoxyphenyl, which behave as electron donors. These results indicate the formation of a D-A framework, which facilitates inter- and intra-molecular electronic transitions, a critical factor for efficient charge transport in semiconducting materials.

Below and above the Fermi level in the PDOS, the p orbitals of the TzTz and the tail molecules are overlapping within the same energy ranges indicating the covalent-like interaction between them. These interactions often result in delocalized π-electrons that enhance electronic conductivity and can

Chemistry–A European Journal

Research Article
doi.org/10.1002/chem.202501664

**Chemistry
Europe**
European Chemical
Societies Publishing

significantly influence the VBM and CBM. Among all the ten crystal structures studied, the four of them: **A2**, **A3**, **A4**, and **B3** are showing the direct-band gap p-type semiconductor where the VBM and CBM are at the same position, and the remaining six compounds: **A1**, **A5**, **B1**, **B2**, **B4**, and **C** feature an indirect band gap with VBM and CBM at different locations.

2.4. Spectral Analysis

2.4.1. Fourier-transformed infrared (FTIR) and Nuclear Magnetic Resonance (NMR) Studies

The solution NMR spectra of TzTzs are technically challenging to obtain due to the compounds' limited solubility in most common deuterated solvents. Nevertheless, we attempted to measure the spectra for all compounds and assigned all proton and carbon signals in their molecules. The NMR spectra, including ^{1}H, ^{13}C, and ^{19}F (where applicable) assignments, are provided in the Supplementary Information as Table S7.

The FTIR spectra of compounds containing the TzTz system were analyzed by comparing the experimental spectra with theoretical spectra calculated using the DFT approach at the B3LYP/TZVP level of theory. This approach enables a more precise assignment of characteristic bands and a deeper understanding of differences arising from intermolecular interactions and specific chemical structural features. Again, characterizing these compounds is challenging due to the presence of numerous overlapping and complex bands in their spectra, which result from the coexistence of conjugated aromatic and heteroaromatic rings.[47] Despite these difficulties, it is possible to distinguish the characteristic bands associated with the TzTz system and the substituents. For the FTIR experimental and theoretical spectra, please refer to Table S8, and for the assignments of the characteristic absorptions, please refer to Tables S9, S10.

As with other aromatic compounds, the TzTz ring exhibits bands corresponding to the asymmetric and symmetric stretching vibrations of C—H bonds. These bands are observed in the range of 3113–3006 cm^{-1} in experimental spectra and 3252–3134 cm^{-1} in calculated spectra.[48] In compounds **A3** and **A4**, which contain —OH groups, the $\nu_{aromC-H}$ overlaps with the stretching vibration mode of the O—H group (Table S8). For compound **A4**, it was not possible to isolate the ν_{O-H}, which is frequently true for hydroxyl groups involved in intramolecular hydrogen bonds.[49] For compound **A5**, the broad and intense ν_{O-H} mode is centered at 3267 cm^{-1},[50] which confirms the formation of a chain of hydrogen bonds with high proton polarizability along crystallographic axis b.[51] In the theoretical spectra, the O—H stretching vibration band appears at 3335 cm^{-1} for **A4** and 3749 cm^{-1} for **A5**. For compounds **A3** and **A4**, symmetric and asymmetric vibrations of methyl groups (from —OCH$_3$) are also observed, appearing in the range of 2968–2835 cm^{-1} in the experimental spectra.[52] In theoretical spectra, these bands shift to higher frequencies, appearing in the range of 3200–3019 cm^{-1}.

Among compounds containing five-membered, heteroaromatic rings, compound **B4** is particular, and its stretching modes corresponding to N—H and C—H aromatic vibrations are significantly broadened and shifted, covering the wide range of 3060–2537 cm^{-1}. In contrast, the theoretical spectra exhibit only two distinct bands: N—H stretching vibrations at 3637 cm^{-1} and C—H at 3253 cm^{-1}.[47,53] These discrepancies arise due to the neglect of intermolecular interactions by computational methods. The broadening of the ν_{N-H} modes is attributed to the properties of the imidazole fragment, which, similar to the hydroxyl group in **A5**, participates in a chain of N—H···N hydrogen bonds along the crystallographic c axis (see also Figure 7). When the imidazoyl substituent is replaced with furyl, thiazoyl, or tienyl, a significant decrease in the intensity of these bands is observed, emphasizing the crucial role of hydrogen bonding in shaping the spectrum.

The most challenging to identify and characterize are the vibrational bands of the TzTz ring, particularly the stretching vibrations of C=C and C=N, which occur in overlapping regions. C=C vibrations are located in the ranges 1679–1549 cm^{-1} and 1450–1410 cm^{-1},[54] while C=N vibrations for most compounds are observed in the range of 1558–1496 cm^{-1} which is much lower than reported in the literature.[55] In the experimental spectra of compounds **A3** and **B3**, it is not possible to unambiguously assign the band corresponding to C=N vibrations. In compound **B4**, these vibrations occur at lower frequencies, between 1485–1431 cm^{-1}. Comparison of experimental and theoretical spectra played a key role in the correct assignment of these bands — most importantly, we have assumed that the order of the bands was not reversed in the results of the calculations, and we have compared the intensity of calculated and experimental bands. Another characteristic feature of the FTIR spectrum is the strong stretching vibration of the C—N bond, appearing in the range of 1397–1219 cm^{-1}.[54c,55] Interestingly, in this case, the band is exceptionally distinct, whereas in most organic compounds, it is typically less noticeable. Moreover, the intensity of this band increases with the number of nitrogen atoms in the molecule.

In the range of 1220–1070 cm^{-1}, FTIR spectra exhibit C—H deformation vibrations, predominantly of the scissoring type, characteristic of aromatic rings and specific substituted phenol groups. In compounds **A2** and **A3**, a very intense C—F stretching vibration band, originating from the CF$_3$ group, is also observed. In experimental spectra, this band appears in the range of 1109–1084 cm^{-1}, while in computed spectra, it is found in the range of 1119–1131 cm^{-1}.[56] The C—F bond is very strong, and fluorine groups are characterized by low polarizability and bond rigidity, limiting their impact on the activation of infrared bands, especially for —CF$_3$ groups.[57] For compounds **A4**, **A5** and furyl derivative **B1**, strong C—O and C—O—C stretching vibrations are observed in the ranges of 1238–1200 cm^{-1} and 1021 cm^{-1}, associated with the presence of —OCH$_3$, —OH and C—O—C groups.[50a,58] The presence of these modes is easily recognized due to their strong intensity and band broadening. In the range of approximately 1000 to 650 cm^{-1}, numerous C—H deformation vibrations of aromatic rings dominate.[59] Additionally, one of the few shared features includes weak-intensity bands attributed to C—S vibrations in thiazole or thiophene rings, observed in the range of 710–529 cm^{-1}.[48a,54a,60]

Chemistry–A European Journal

Research Article
doi.org/10.1002/chem.202501664

Chemistry
Europe
European Chemical
Societies Publishing
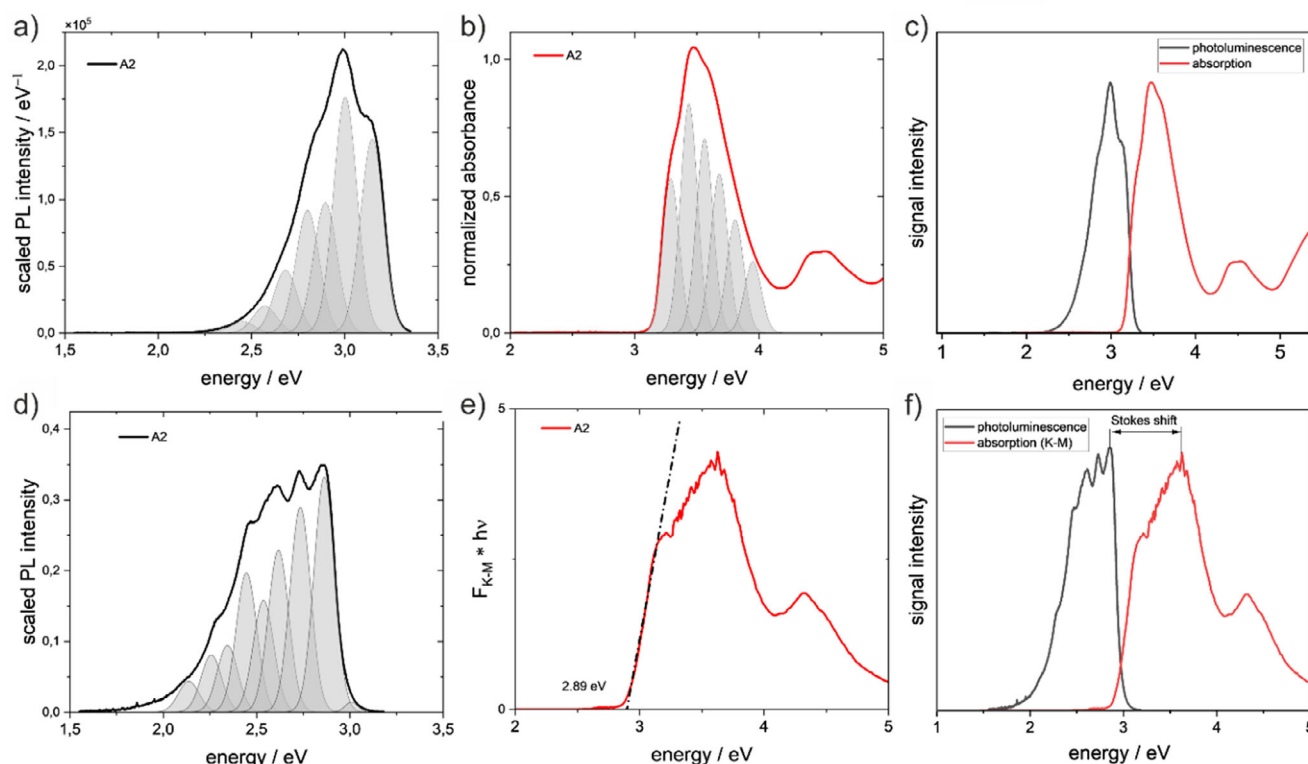
Figure 13. Spectroscopic UV-Vis range overview of the **A2** compound. The Upper row presents results for the MeCN solution of the compound: a) emission spectrum b) absorption spectrum c) Stokes shift. The Bottom row presents results for powdered sample: d) emission spectrum e) Kubelka-Munk plot f) Stokes shift.

2.4.2. Ultraviolet-Visible (UV-Vis) Range: Absorption and Photoluminescence Studies

The analysis of UV-Vis spectra in solution for all compounds reveals absorption maxima ranging from 3.10 eV (400 nm) for **C** to 3.50 eV (354 nm) for **A1** and **A3**, while in the solid state, the bandgaps range from 2.34 eV (530 nm) for **A4** to 2.91 eV (426 nm) for **A3**. Emission maxima in solution span from 2.61 eV (474 nm) for **C** to 3.03 eV (409 nm) for **A1**. The TzTz compounds were also emissive in the solid state, except for the **B4** compound. The correlation between absorption and emission maxima for an exemplary TzTz derivative, **A2**, along with other UV-Vis spectral features, is shown in Figure 13. Similar spectra for other compounds are provided in Figure S7 (A-type compounds) and Figure S8 (B- and C-type compounds). In all cases, the lowest energy transition has a $\pi-\pi^*$ (HOMO→LUMO) transition and is in good agreement with theoretically predicted spectra (Figure S10, Table S11).

Comparison of the Stokes shift for the same compound measured in MeCN and in solid state revealed a consistent trend of increased values for solid-state measurements. Substantial increases in Stokes shift were observed for **A1**, **A2**, **A5**, **B1**, **B2**, and **C**. This phenomenon occurs due to the increased intermolecular interactions or structural distortions in solid state[61] especially when it comes to planar structures, which can experience π-conjugation in solid state,[62] which results in emission maxima redshift (toward lower energies). At the same time presence of specific functional groups can affect this shift, lead-

ing to more efficient nonemissive energy dissipation from the excited states. High Stokes shifts are advantageous for minimizing reabsorption of emitted photons, which is beneficial for optoelectronic applications.[63] Here Stokes shifts of ca. 0.4 eV in solution and up to 1 eV in the solid phase can be achieved despite low dipole moment difference between ground and excited states of the chromophore (fully symmetrical HOMO and LUMO orbitals, cf. Table 3), which contradicts the Lippert-Mataga rule.[64]

Spectra in solution (MeCN) and in the solid state exhibit visible broadening, which may be attributed to oscillation broadening or vibrational progression. To analyze this effect, each spectrum was deconvoluted into Gaussian functions. The energy differences between peaks constituting the main spectral features were measured to assess the oscillation broadening of the bands for each type of spectrum: absorption spectrum in MeCN and emission spectrum in MeCN and the solid state. All calculated mean values are presented in Table 5. Similarly, strongly expressed vibrational progression has been reported for the **A1** and also the TzTz molecule itself.[65] Broadening of the absorption peak in the spectrum measured in MeCN ranges from 0.11 eV to 0.16 eV, which is equivalent to 869.8 cm^{-1} and 1258.3 cm^{-1} and can be identified in the IR spectrum as oscillations related to deformation of the TzTz core unit. It should be noted that the TzTz core usually shows a series of similar distorting vibrations resulting from coupling with different vibrational modes of substituents. This is the reason for slightly different vibronic progression patterns for absorption and emission spectra.

Chemistry–A European Journal

Research Article
doi.org/10.1002/chem.202501664

Chemistry Europe
European Chemical
Societies Publishing

Table 5. Parameters describing spectrum broadening and vibrational progression.

	Code	A1	A2	A3	A4	A5
abs MeCN	Energy difference [eV]	0.12	0.14	0.12	0.14	0.13
	Energy difference [cm^{-1}]	957	1161	1007	1114	1071
	Vibration mode (DFT)	974	1247	1028	1124	1047
em MeCN	Energy difference [eV]	0.11	0.12	0.12	0.11	0.13
	Energy difference [cm^{-1}]	882	938	929	898	1009
	Vibration mode (DFT)	880	977	919	930	1023
em solid state	Energy difference [eV]	0.11	0.10	0.16	0.16	0.17
	Energy difference [cm^{-1}]	875	804	1276	1291	1400
	Vibration mode (exp)	880	809	1283	1248	1423
	Code	**B1**	**B2**	**B3**	**B4**	**C**
abs MeCN	Energy difference [eV]	0.13	0.12	0.11	0.16	0.14
	Energy difference [cm^{-1}]	1082	967	870	1258	1129
	Vibration mode (DFT)	1020	973	880	1294	1200
em MeCN	Energy difference [eV]	0.10	0.10	0.10	0.13	0.13
	Energy difference [cm^{-1}]	832	846	823	1035	1083
	Vibration mode (DFT)	851	854	835	1041	1198
em solid state	Energy difference [eV]	0.18	0.13	0.15	-	0.12
	Energy difference [cm^{-1}]	1424	1036	1200	-	944
	Vibration mode (exp)	1436	1054	1240	-	943

Electronic excitation thus does not initiate any strong distortion in molecular geometry. These values are more high-energy than the one reported for the TzTz unit, which is due to the additional molecular mass in the form of functional groups in symmetrical configuration. The same outcome happens for each of the analyzed compounds. This fact shows that the TzTz core acts as the main chromophore, which can also be concluded from the previously presented PDOS analysis. At the same time, a good correlation between predicted (DFT) and registered (FT-IR) frequencies has been observed. Vibrational progression is similar for the same compounds in solution for absorption and emission with the highest difference over 200 cm^{-1} reported for **A2**, **A4**, **B1**, and **B4**. It indicates that the same oscillation is influencing electronic state transitions. Comparison of emission data for solution and solid state shows that most significant differences in vibrational modes happen for **B1** (591 cm^{-1}), **A3**, **A4**, and **A5** (more than 340 cm^{-1} difference). The dataset describing spectrum broadening is presented in the form of Table 5 and can be compared with Figure S11 and S12, where deconvoluted spectra are shown.

More detailed analysis of diffuse reflectance spectra has been performed on the basis of the Tauc method. First, diffuse reflectance spectra were converted to the Kubelka-Munk function, defined as follows (Equation 4):

$$F(R) = \frac{(1 - R)^2}{2R} \tag{4}$$

where R is the reflectance. For powder samples dispersed in scattering media, it is commonly assumed that F(R) is proportional to the absorption coefficient α.[66] Then the Tauc function

has been applied to fit the linear fragment of the spectrum (Equation 5):[67]

$$(\alpha \cdot h\nu)^{\frac{1}{r}} = A\left(h\nu - E_g\right) \tag{5}$$

where A is the proportionality constant (independent of the photon energy), h is the Planck constant, ν is the photon frequency, E_g is the band gap, α is the absorption coefficient, and r is the exponent describing the nature of the band gap: $r = \frac{1}{2}$ for direct and $r = 2$ for indirect transitions, respectively.[67]

In the case of amorphous (or almost amorphous) material, it is assumed that $r = 1$ seems to be the most reasonable choice.[68] The same approximation is commonly used for molecular crystalline materials as well as for ionic crystals with only a weak covalent interaction between ionic species.[69] Despite the fact that DFT models predict both direct and indirect band gaps, the $r = 1$ case provides the best fit for the spectra, which is consistent with relatively weak intermolecular interactions in covalent crystals. Therefore, the final equation that allows the determination of the band gap is derived as follows (Equation 6):

$$F(R) \cdot h\nu = A\left(h\nu - E_g\right) \tag{6}$$

Optical band gaps, along with other spectroscopic parameters, are collated in Table 6. Fitted parameters for bandgap determination are presented in Table S12.

2.4.3. Lifetime Measurements

For photoluminescence lifetime measurements in solid state at RT, in almost each case a two-exponential fit was calculated,

Chemistry–A European Journal

Research Article
doi.org/10.1002/chem.202501664

Chemistry
Europe
European Chemical
Societies Publishing

Table 6. UV-Vis spectroscopic parameters alongside optical bandgaps and lifetimes.

Code	Substituent	MeCN solution				Solid state				
		Max abs [eV]	Max em [eV]	Stokes shift [eV]	Lifetime [ns]	Band gap [eV]	Max abs [eV]	Max em [eV]	Stokes shift [eV]	Life time [ns]
A1		3.50	3.03	0.47	$\tau_1 = 0.2428$ $\tau_2 = 0.5205$ $\chi^2 = 1.124$	2.89	3.48	2.67	0.81	$\tau_1 = 0.7844$ $\tau_2 = 1.9463$ $\chi^2 = 1.093$
A2		3.47	2.99	0.48	$\tau_1 = 0.266$ $\tau_2 = 0.581$ $\chi^2 = 2.641$	2.89	3.63	2.85	0.78	$\tau_1 = 0.246$ $\tau_2 = 0.721$ $\chi^2 = 1.14$
A3		3.50	3.01	0.49	$\tau_1 = 0.241$ $\tau_2 = 0.457$ $\chi^2 = 1.017$	2.91	3.32	2.70	0.62	$\tau_1 = 1.803$ $\tau_2 = 4.488$ $\chi^2 = 1.290$
A4		3.32	2.98	0.34	$\tau_1 = 0.269$ $\tau_2 = 0.489$ $\chi^2 = 1.174$	2.34	3.11	2.00	1.11	$\tau_1 = 0.257$ $\tau_2 = 1.125$ $\chi^2 = 1.005$
A5		3.31	2.80	0.51	$\tau_1 = 0.204$ $\tau_2 = 0.652$ $\chi^2 = 1.084$	2.61	3.24	2.43	0.81	$\tau_1 = 0.246$ $\tau_2 = 1.857$ $\chi^2 = 1.323$
B1		3.34	2.88	0.46	$\tau_1 = 0.303$ $\tau_2 = 0.566$ $\chi^2 = 1.310$	2.72	2.93	2.13	0.80	$\tau_1 = 0.719$ $\tau_2 = 1.856$ $\chi^2 = 1.019$
B2		3.23	2.77	0.46	$\tau_1 = 0.282$ $\tau_2 = 0.542$ $\chi^2 = 1.171$	2.57	3.04	2.33	0.71	$\tau_1 = 0.507$ $\tau_2 = 1.200$ $\chi^2 = 1.078$
B3		3.21	2.79	0.42	$\tau1 = 0.344$ $\tau2 = 0.659$ $\chi2 = 1.514$	2.61	3.00	2.35	0.65	$\tau1 = 1.419$ $\tau2 = 2.842$ $\chi2 = 1.115$
B4		3.33	2.86	0.47	$\tau1 = 1.052$ $\tau2 = 2.123$ $\chi2 = 1.323$	2.62	3.15	-	-	-
C		3.10	2.61	0.49	$\tau_1 = 0.818$ $\chi^2 = 1.651$	2.40	1.99	3.04	1.05	$\tau_1 = 0.588$ $\tau_2 = 1.748$ $\chi^2 = 1.161$

with χ^2 parameters being below 1.3 (Table 6). An exception was observed for compound **C** in MeCN, where the photoluminescence lifetime was described by single-exponential decay. Analysis of τ_1 across compound types (**A1-A5**, **B1-B4**, and **C**) revealed variability between solution and solid state. Some of the compounds (**A3, B4**) exhibit substantial increases in photoluminescence lifetimes, while others (**A2, A4**) show slight decreases or only minimal changes, suggesting limited variation in their emissive properties between solution and solid-state forms. In contrast, τ_2 consistently increases for solid state across nearly all examples. Specifically, **A3** and **B3** showed the most pronounced increases in both τ_1 and τ_2, into long-lived fluorescence lifetimes of the order of ns.

These observations align with the photoluminescence phenomena principles, where the solid-state environment often promotes extended lifetimes due to decreased rates of non-radiative decay. The results underline the importance of both molecular structure and neighboring environment in determining photoluminescence — which must be taken into account upon development of materials for solid-state optoelectronic applications.

It is worth noticing that the powder samples exhibited much longer lifetimes than their solution counterparts. For most compounds, the lifetimes determined for solutions are twice as short as for solid samples. Only for samples **A2, A4,** and **A5**, the lifetimes are comparable. The longest time for solid samples is expected since bulk organic aggregates require higher reorganization energy than molecular monomers in dilute solutions.[11a] This also explains Stoke shifts, which are significantly larger in the case of solid samples.

Chemistry–A European Journal

Research Article
doi.org/10.1002/chem.202501664

Chemistry Europe
European Chemical
Societies Publishing

2.5. XAS Analysis

Sulfur exhibits various oxidation states, ranging from -2 to $+6$, forming chemical bonds with elements of differing electronegativities. This significantly influences the local electronic and atomic structure of sulfur, and XAS is an excellent tool for studying these phenomena. Performing XAS measurements of TzTzs at the sulfur K-edge allows researchers to determine the formal oxidation state of the sulfur atom, enabling precise identification of redox states critical for TzTz's stability, analyzing the geometric arrangement of neighboring atoms to define local site symmetry, and obtaining information about unfilled orbitals and their electron populations.

XAS, often exploited combined with synchrotron radiation, is an element-specific technique that probes the electronic structure of a specific element, its local coordination and, the bonding environment. XAS probes electronic transitions of a core electron (1 s for K-edge) to an empty state above Fermi energy. X-ray absorption near edge structure (XANES) part of XAS, typically from ~20 eV below the edge to 50–100 eV above the edge, arises from transitions that may include bound states due to resonant excitations. Extended X-ray absorption fine structure (EXAFS) is a higher-energy oscillatory part of XAS, which may reveal a few coordination spheres around an absorber by analyzing the possible scattering path on adjacent atoms. The XAS measurements presented in this work were performed in transmission mode, which is tricky to realize in soft and tender energy ranges, as for the S K-edge. Spectra measured in transmission mode have reduced artifacts in comparison to spectra measured in fluorescence mode, which are often influenced by self-absorption, a phenomenon whereby the fluorescence detector signal is distorted due to reabsorption of the emitted fluorescence photons by the sample itself. The XAS measurements presented in this work were performed in transmission mode, which eliminates this effect. We believe that the measured spectra of the new TzTz compounds presented in this paper could also be used as reference data for further researches on this topic.

Figure S13 in Supporting Information shows the full XAS spectra, that is, XANES and EXAFS, measured for the studied TzTz derivatives. The spectra differ from each other, which is more evident in the XANES shown in Figure 14. The shape of XANES reflects a complex relationship between charge screening and orbital hybridization effects.[70] Charge screening describes how the local chemical environment of an atom and the surrounding electron density influence the effective nuclear charge felt by the core and valence electrons. Orbital hybridization refers to the mixing of atomic orbitals of the absorber with orbitals from the neighboring atoms. This results in the creation of hybridized orbitals, which may disrupt the electron density of unoccupied states available for the excited core electrons. Hybridization affects the transition probabilities to these final states, thereby influencing features in the X-ray absorption spectrum—most notably, the white line intensity corresponding to transitions into low-lying unoccupied orbitals, often of p-character. This effect is observed in the studied TzTzs, where the white line intensity varies, being the lowest for **A1** and the highest for **A4**. A high white line indicates absorption to localized unoccupied states
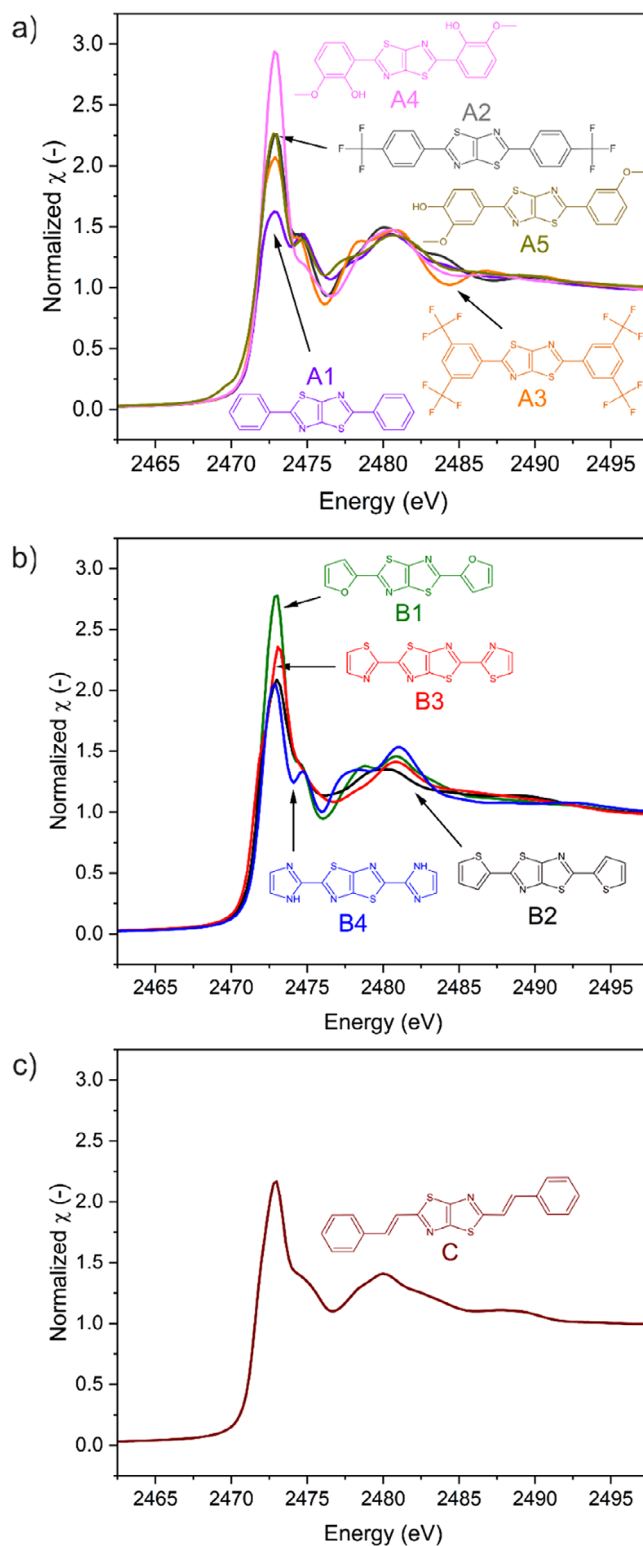
Figure 14. Sulfur K-edge XANES for the studied TzTzs measured in transmission mode: a) **A1**-**A5**; b) **B1**-**B4**; c) **C**.

and weaker hybridization effects. This highlights the subtle interplay between molecular structure, electronic configuration, and X-ray absorption characteristics.

Because of low electron density, the position of the sulfur K absorption edge and the features of the XANES spectra of

Chemistry–A European Journal

Research Article
doi.org/10.1002/chem.202501664

Chemistry Europe
European Chemical
Societies Publishing

Table 7. XAS S K-edge values for parameters for the studied TzTz derivatives.

	E_{edge} [eV]	$E_{white\ line}$ [eV]
A1	2471.8	2472.8
A2	2471.8	2473.0
A3	2471.7	2472.9
A4	2472.0	2472.8
A5	2472.0	2472.8
B1	2472.1	2473.0
B2	2471.7	2473.0
B3	2471.5	2473.1
B4	2472.0	2472.9
C	2471.6	2473.0

these materials are highly sensitive to both charge screening and orbital hybridization effects.

Due to weak charge screening, the position of the sulfur K-edge strongly depends on the oxidation state of this element,[71] as it varies from 2470.4 eV for $CuFeS_2$ (−2 oxidation state) up to 2482.0 eV for Na_2SO_4 (+6 oxidation state).[71,72] For the studied TzTz derivatives, sulfur occurs in a formal −2 oxidation state, resulting in absorption K-edge values between 2471.5 and 2472.1 eV (Table 7). These values may confirm sulfur − 2, as even for simple sulfides with a formal oxidation state of −2, the absorption edge value may vary, for example, 2471.7 eV for HgS, 2471.7 eV for As_2S_3, 2473.2 eV for CaS, and 2473.8 eV for ZnS. The negligible difference in electronegativity between S (2.58) and C (2.55) in TzTzs implies that the bond between these two elements exhibits largely covalent character with minimal polarity. In fact, the absorption edges of the studied TzTzs are closer to covalently bound sulfides (HgS, As_2S_3) than to ionic ones (CaS, ZnS), which is consistent with the covalent character of the C—S bond. Therefore, precise analysis of the oxidation state of materials using XANES spectra relies on comparing the absorption edge positions of samples where the absorbing atom is surrounded by ligands of the same type. Moreover, in the case of TzTz, the formal oxidation state may not be sufficient to understand the bonding environment and electron distribution in these compounds.

In S K-edge, the main electronic transitions occur according to the Laporte rule allowing for the dipole transitions with orbital quantum number $\Delta l = \pm 1$. The basic electron configuration of sulfur is [Ne] $3s^2\ 3p^4$, but the one expected for TzTzs with a −2 oxidation state is a closed shell [Ne] $3s^2\ 3p^6$, as for Ar. Herein, the most probable transition is from 1 s sulfur orbital to σ^* and π^* anti-bonding molecular orbitals formed with the neighboring atoms. Therefore, orbital hybridization should play an important role in shaping the near-edge structure. To study the orbital hybridization in detail, the XAS spectra of the studied TzTzs were also modeled using the Finite Difference Method Near Edge Structure (FDMNES) ab initio code.[73] The experimental and theoretical data are shown for each of the compounds in the Supporting Information in Figure S14. The calculated PDOS, associated with specific molecular orbitals within a material, con-

firms that the sulfur K-edge appears at the electronic transition to 4p orbitals. For different substituents of the TzTz ring, we observe different contributions from the p_x, p_y, and p_z orbitals to the PDOS. Substituents with electron-donor character (**A4**, **A5**, **B2**, **B4**) tend to have lower energy $4p_z$ orbitals compared to $4p_x$ and $4p_y$. On the other hand, substituents with electron-acceptor character (**A1**, **A2**, **B3**) have lower energy $4p_x$ orbitals. The substituent in **C** is the only one connected via a vinylene π bridge to the TzTz ring and also is the only one with the low energy $4p_y$ orbital.

2.6. Electric Measurements

Representatives **A4**, **A5**, **B3**, **B4**, and **C** were selected based on their superior solubility in DMF compared to the remaining compounds, which are almost insoluble in DMF or other solvents suitable for spin-coating. Layered devices were prepared, and their current — voltage (I-V) characteristics were measured across varying temperatures, as shown in Figure 15. The I-V responses remained stable for all compounds between − 20 °C and 120 °C. The forward-to-reverse bias current amounts to 1.07 ± 0.08 (average value for all compounds), the highest for **A5** (1.18) and the lowest for **C** (1.0). Furthermore, the current-voltage dependencies are almost linear, with slopes almost identical for both low and high temperatures. It indicates the lack of Schottky barrier at the copper/TzTz interface. On the other hand formation of metallic filaments can be excluded due to a small resistivity change during switching. Therefore, the only reasonable mechanistic explanation will be an electron injection-enhanced electron hopping mechanism. This hypothesis is supported by much higher electron coupling matrix elements $|H_{DA}|$ (cf. Equation 1) for negatively charged dimers as compared with neutral ones (cf. Table 4). This observation is consistent with other molecular crystal organic[46] and organometallic[28] semiconductors. Basic endurance and retention tests, which are presented in the Supplementary Information, revealed that while three out of five (**A5**, **B3,** and **C**) compounds maintained distinct high-resistance (HRS) and low-resistance (LRS) states, their endurance and stability varied significantly for each of them.

For **A4**, the resistive states remained separated during 750 on-off cycles but diminished toward convergence into a single state, indicating instability during both cycling and retention evaluations. In contrast, **A5** exhibited consistent separation of HRS and LRS throughout the 750 cycles, with no degradation in performance upon switching, thus demonstrating sufficient stability.

Compound **B3** displayed diminishing state separation after 750 cycles, aligning with the narrow hysteresis curve observed in Figure S15. State retention for **B3** was reliable over the 2-hour test. Compound **B4** showed indistinguishable resistive states after 100 cycles and lost retention within 2 hours, suggesting that it may be better suited for volatile memory or dynamic signal applications. Similarly, compound **C** maintained distinct resistive states only up to 300 cycles, highlighting its potential for low-duty-cycle applications. These results, only for exemplary compounds from each group show diversity in charge transport
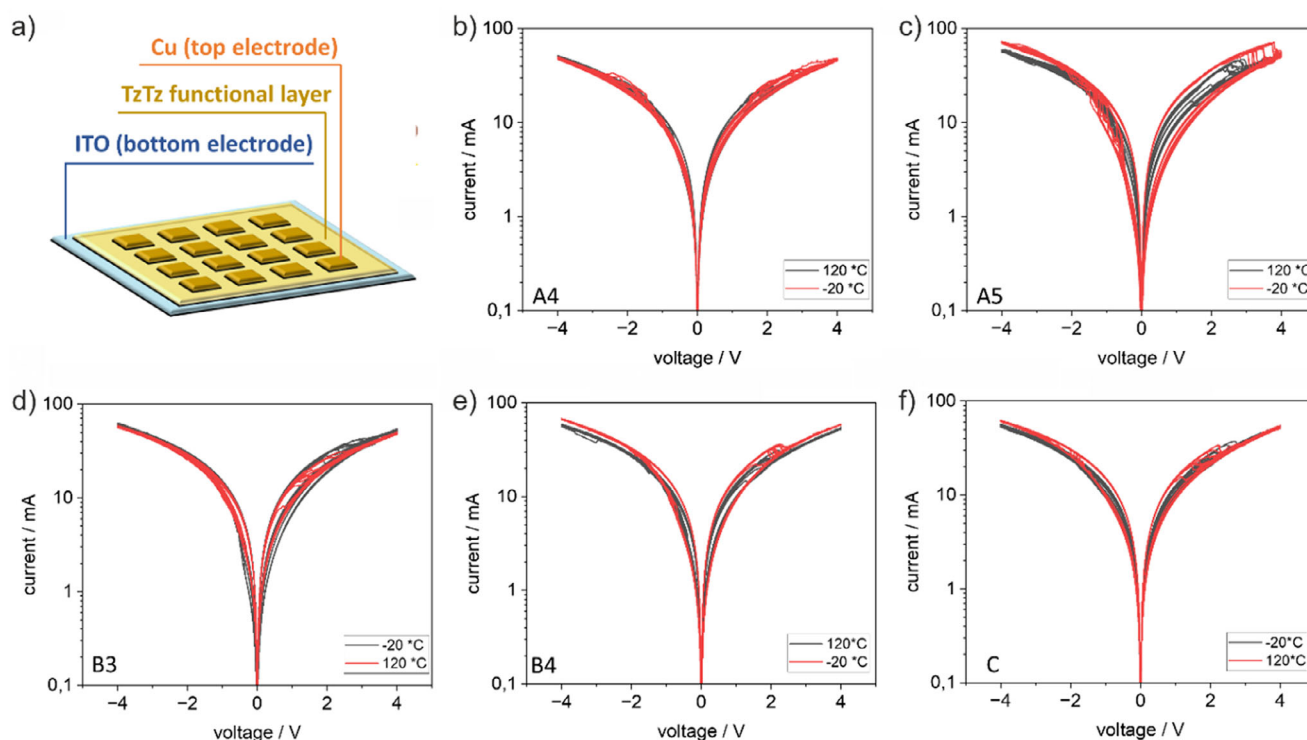
Figure 15. Temperature-dependent current-voltage I-V characteristics for the selected TzTzs: a) Scheme of the device; b) **A4**; c) **A5**; d) **B3**, e) **B4**; f) **C**.

mechanisms. As such TzTzs, are offering a range of switching characteristics that can be fine-tuned for specific technological requirements. However, other parameters, such as the on-off ratio need to be refined before introducing the compound for industrial applications (Figure S16).

From a neuromorphic perspective, **A4** demonstrated basic plasticity behaviors such as depression and potentiation at threshold pulse values of 1.6 V, suggesting its potential use in synaptic plasticity change-based learning models. Results for **A4** and other compounds are presented in Figure 16. **A5** required higher pulse voltages, 2.4 V of higher for switching, reflecting a more energy-intensive but highly stable device suitable for neural networks.

Compound **B3** exhibited dynamic switching responses from 1.6 V with steep but gradual changes, indicating its suitability for spiking neural network simulations. **B4** can operate on pulses higher or equal to 1.2 V, however poor retention of the states causes instability of the responses. Compound **C**, with dynamic responses initiated at lower voltages (1.2 V pulses), shows promise for low-power neuromorphic applications, though its limited endurance suggests constraints in high-voltage regimes.

Overall, the presented behaviors across these compounds highlight their adaptability for different memristive and neuromorphic applications. Compounds like **B4** and **C** provide opportunities for volatile memory applications and energy-efficient synaptic emulation, while the increased stability of **A5** makes it a strong candidate for nonvolatile, high-endurance memory systems. This diversity in performance underlines the poten-

tial of TzTz derivatives as versatile materials for next-generation neuromorphic and memristive technologies.

3. Conclusions

TzTz derivatives show great promise for flexible optoelectronic and sensing applications due to their simple one-step synthesis, structural tunability, and rich optical properties. Their well-defined molecular geometry supports $\pi-\pi$ stacking, hydrogen bonding, and chalcogen/halogen interactions, which stabilize the crystal lattice and shape their spectroscopic behavior. A broad range of electron-donating and electron-withdrawing substituents can be introduced, enabling precise control over optical bandgaps and emission profiles.

Three distinct packing motifs—herringbone, parallel, and grid—were identified among the studied compounds, influencing intermolecular electronic interactions. Despite this, XAS spectra reveal consistent molecular-level scattering patterns, with white line intensity variations hinting at differences in orbital delocalization.

Electrical characterization revealed that soluble derivatives **A4**, **A5**, **B3**, **B4**, and **C** exhibit stable, temperature-independent conductivity and hysteresis suitable for memristive purposes. Among them, only **A5** and **B3** demonstrated reliable, reversible switching, with **A5** showing long-term stability under repeated cycling.

Looking ahead, functionalization through metal coordination is expected to enhance their electronic and optical features

Chemistry–A European Journal

Research Article
doi.org/10.1002/chem.202501664

Chemistry
Europe
European Chemical
Societies Publishing
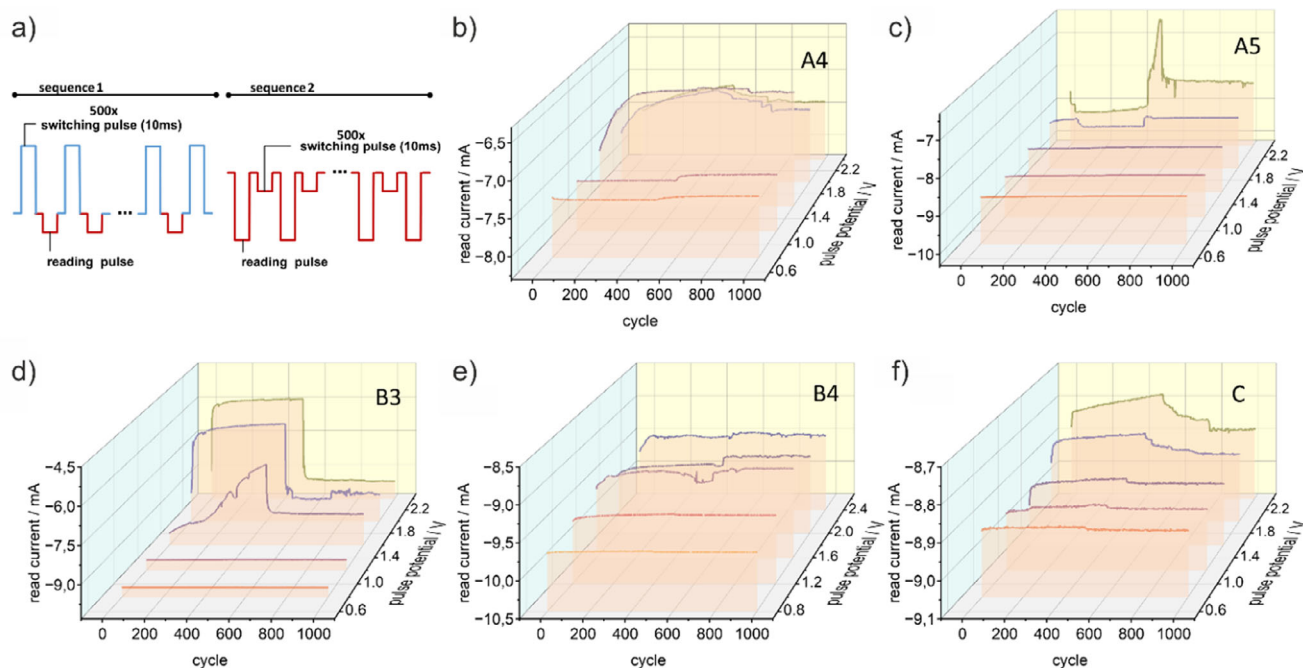
Figure 16. The potentiation depression measurements for the selected TzTzs; basic plasticity features for various potential pulses: a) pulse sequence for the measurements; b) **A4**; c) **A5**; d) **B3**; e) **B4**; f) **C**.

further. Overall, TzTz compounds offer a versatile platform for designing advanced materials via straightforward synthesis and rational substitution strategies.

4. Experimental

Synthetic procedures: The following chemicals were used as purchased: benzaldehyde, 98%, Thermo Scientific (Alfa Aesar); 4-(trifluoromethyl)benzaldehyde, 98%, Sigma-Aldrich; 3,5-bis(trifluoro-methyl)benzaldehyde, 97%, Sigma-Aldrich; 2-hydroxy-3-methoxy-benzaldehyde, 99%, Sigma-Aldrich; 4-hydroxy-3-methoxybenzalde-hyde, 99%, Thermo Scientific (Alfa Aesar); 2-Furaldehyde, 98%, Thermo Scientific (Alfa Aesar); 2-Thiophenecarboxaldehyde, 98%, Sigma-Aldrich; 2-Thiazolecarboxaldehyde, 98%, Sigma-Aldrich, 2-imidazolecarboxaldehyde, 97%, Angene; Cinnamaldehyde, 97%, Sigma-Aldrich, N,N-dimethylformamide (DMF), p., POCh; ethanol (EtOH), 99.9%, POCh; dichloromethane (DCM), p., POCh; 1-methylptrrolidine, 98%, Sigma-Aldrich.

All TzTzs were synthesized following a uniform procedure. The compounds were obtained by mixing the substrates in a molar ratio of 1: 2.3 (dithiooxamide: aldehyde), starting with 1 g of dithiooxam-ide. The mixture was dissolved in 30 mL of DMF and heated at the appropriate temperature (see below).

2,5-bis(phenyl)-1,3-thiazolo[5,4-d]-1,3-thiazole (A1): The reaction mixture was heated at 140–145 °C for 1.5 hours. Yellowish, crys-talline product was obtained in the form of blocks; yield 69% (based on dithiooxamide), m.p. 209–213 °C. Elemental analysis (%): calcd C 65.27, H 3.42, N 9.52; found C 65.25, H 3.40, N 9.53.

FT-IR ATR: 3061(w), 3014(w), 1953(w), 1881(w), 1824(w), 1750(w), 1679(w), 1600(w), 1501(m), 1456(s), 1430(s), 1336(w), 1309(s), 1219(m), 1199(w), 1164(w), 1100(w), 1071(w), 1031(m), 1006(m), 996(m), 910(w), 883(w), 754(s), 680(s), 637(w), 611(s), 483(w) cm^{-1}.

NMR: ^{1}H NMR (400 MHz, CDCl$_3$-d_1): δ = 8.02–7.97 (m, 4H, *ortho*-C-H (H$_o$)), 7.51–7.44 (m, overlapped, 6H, *meta*-C-H and *para*-C-H (H$_m$ and H$_p$)); ^{13}C{^{1}H} NMR (100 MHz, CDCl$_3$-d_1): δ = 169.21 (s, S**C**N (**C2**)), 150.86 (s, **C** = **C** (**C1**)), 133.94 (s, **C**$_i$ (**C3**)), 130.71 (s, *meta*-**C**H (**C6**)), 129.16 (s, *para*-**C**H (**C5** and **C7**)), 126.45 (s, *ortho*-**C**H (**C4** and **C8**))

2,5-bis(4-trifluoromethylphenyl)-1,3-thiazolo[5,4-d]-1,3-thiazole (A2): The reaction mixture was heated at reflux for °C for 18 hours. A greenish-yellow crystalline product was obtained and purified in 30 mL of dichloromethane, yield 35% (based on dithiooxamide), m.p. 269.9–264.9 °C. Elemental analysis (%): calcd C 49.99, H 2.33, N 6.48; found C 49.98, H 2.35, N 6.50.

FT-IR ATR: 3083(w), 3055(w), 1941(w), 1889(w), 1590(w), 1570(w), 1496(m), 1436(s), 1397(s), 1319(w), 1291(w), 1222(m), 1199(w), 1168(w), 1103(w), 1085(s), 1014(m), 1006(s), 974(w), 881(m), 839(s), 809(s), 729(w), 711(w), 659(m), 621(m), 613(m), 516(m), 497(m), 459(w) cm^{-1}.

NMR: ^{1}H NMR (400 MHz, CDCl$_3$-d_1): δ = 8.13 (d, ^{3}J$_{HH}$ = 8, 2H, *ortho*-C-H (H$_o$)), 7.58 (d, ^{3}J$_{HH}$ = 8, 2H, *meta*-C-H (H$_m$)); ^{13}C{^{1}H} NMR (100 MHz, CDCl$_3$-d_1): δ = 167.9 (s, S**C**N (**C2**)), 151.8 (s, **C** = **C** (**C1**)), 136.9 (s, **C**$_i$ (**C3**)), 132.4 (m*, ^{2}J$_{CF}$ = 33, **C**CF$_3$ (**C6**)) 126.7 (br s, *ortho*-**C**H (**C4** and **C8**)), 126.2 (q, ^{3}J$_{CF}$ = 4, *meta*-**C**H (**C5** and **C7**)), 123.7 (m*, ^{1}J$_{CF}$ = 272, **C**F$_3$); *m - Expected to be a quartet, but due to the low solubility of the compound, it is not clearly visible. ^{19}F NMR (376 MHz, CDCl$_3$-d_1): δ = − 62.9 (s, **C**F$_3$).

2,5-bis{bis(3,5-trifluoromethyl)phenyl}-1,3-thiazolo[5,4-d]-1,3-thiazole (A3): The reaction mixture was heated at reflux for 18 hours. Greenish-yellow crystalline product was obtained and purified in 30 mL of dichloromethane, yield 42%, m.p. 263.5–264.5 °C. Elemental analysis (%): calcd C 41.67, H 2.80, N 4.86; found C 41.70, H 2.81, N 4.83.

FT-IR ATR: 3113(w), 1619(w), 1484(w), 1436(w), 1360(s), 1325(w), 1283(s), 1217(m), 1164(s), 1109(s), 1041(s), 918(m), 897(s), 846(m), 776(w), 706(w), 698(m), 684(m), 654(w), 448(w) cm^{-1}.

NMR: ^{1}H NMR (400 MHz, CDCl$_3$-d_1): δ = 8.46 (s, 4H, *ortho*-**C**H (H$_o$)), 7.99 (s, 2H, *para*-**C**H (H$_p$)); ^{13}C{^{1}H} NMR (100 MHz, CDCl$_3$-d_1): δ = 166.5 (s, S**C**N (**C2**)), 152.0 (s, **C** = **C** (**C1**)), 135.5 (s, **C**$_i$ (**C3**)), 132.9 (q, ^{2}J$_{CF}$ = 34, **C**CF$_3$ (**C5** and **C7**)), 126.4 (br s, *ortho*-**C**H (**C4** and **C8**)), 124.1 (m, *para*-**C**H (**C6**)), 122.9 (m*, ^{1}J$_{CF}$ = 273, **C**F$_3$), *m - Expected to be a quartet, but due to the low solubility of the compound, it is not clearly visible. ^{19}F NMR (376 MHz, CDCl$_3$-d_1): δ = − 63.0 (s, **C**F$_3$);

Chemistry–A European Journal

Research Article
doi.org/10.1002/chem.202501664

Chemistry Europe
European Chemical
Societies Publishing

2,5-bis(2-hydroxy-3-methoxyphenyl)-1,3-thiazolo[5,4-d]-1,3-thiazole (A4): The reaction mixture was heated at 120–125 °C for 4–6 hours. A yellow crystalline product in the form of thin needles was obtained and purified in 30 mL of ethanol; yield 48,19% (based on dithiooxamide); m.p. 288 °C. Elemental analysis (%): calcd C 55.94, H 3.65, N 7.25, S 16.60; found C 55.95, H 3.65, N 7.33, S 16.49.

FT-IR ATR: 3006(w), 2968(w), 2835(w), 1584(w), 1502(w), 1561(s), 1443(s), 1415(s), 1248(s), 1171(m), 1115(m), 1094(m), 1021(s), 924(w), 870(w), 832(w), 777(s), 718(s), 678(m), 626(w) cm^{-1}.

NMR: ^{1}H NMR (400 MHz, DMSO-d_6): δ = 10.68 (bs, 2H, **OH**), 7.84 (d, overlapped, $^3J_{HH}$ = 8, 2H, *ortho*-C-**H** (**H$_o$**)), 7.12 (d, overlapped, $^3J_{HH}$ = 8, 2H, *para*-C-**H** (**H$_p$**)), 6.97 (t, $^3J_{HH}$ = 8, 2H, *meta*-C-**H** (**H$_m$**)), 3.89 (s, 6H, **CH$_3$**);^{13}C{^{1}H} NMR (100 MHz, DMSO-d_6): δ = 164.34 (s, SCN (**C2**)), 151.14 (s, **C**=**C** (**C1**)), 148.91 (s, **C**-OCH$_3$ (**C5**)), 145.31 (s, **C**-OH (**C4**)), 120.82 (s, **C$_i$** (**C3**)), 119.97 (s, **C**H$_m$ (**C7**)), 119.44 (s, **C**H$_o$ (**C8**)), 113.68 (s, **C**H$_p$ (**C6**)), 56.8 (s, **C**H$_3$).

2,5-bis(4-hydroxy-3-methoxyphenyl)-1,3-thiazolo[5,4-d]-1,3-thiazole (A5): The reaction mixture was heated at 120–125 °C for 4–6 hours. An orange powder was obtained and purified in 30 mL of ethanol; yield 33,41% (based on dithiooxamide); m.p. 275–280 °C. Elemental analysis (%): calcd C 55.95, H 3.65, N 7.25, S 16.49; found C 55.80, H 4.01, N 7.19, S 16.42.

FT-IR ATR: 3525(m), 3396(s), 2990(w), 2943(w), 2879(w), 2834(w), 1667(w), 1596(m), 1520(s), 1466(s), 1445(w), 1432(s), 1376(w), 1290(m), 1264(s), 1246(s), 1217(s), 1191(m), 1137(m), 1112(m), 1024(m), 857(w), 839(m), 820(m), 795(m) cm^{-1}.

NMR: ^{1}H NMR (400 MHz, DMSO-d_6,): δ = 9.82 (bs, 2H, **OH**), 7.54 (s, overlapped, 2H, *ortho*-C**H** (**H1**)), 7.45 (m, overlapped, 2H, *ortho*-C**H** (**H2**)), 6.92 (d, $^3J_{HH}$ = 8 Hz, 2H, *meta*-C**H** (**H3**)), 3.84 (s, 6H, OCH$_3$); ^{13}C{^{1}H} NMR (100 MHz, DMSO-d_6): δ = 168.75 (s, SCN (**C2**)), 150.17 (s, **C** = **C** (**C1**)), 149.46 (s, **C**-OH (**C6**)), 148.65 (s, **C**-OCH$_3$ (**C5**)), 125.23 (s, **C$_i$** (**C3**)), 120.34 (s, *ortho*-C**H** (**C8**)), 116.45 (s, *meta*-C**H** (**C7**)), 109.78 (s, *ortho*-C**H** (**C4**)), 56.20 (s, **C**H$_3$).

2,5-bis(2-furyl)-1,3-thiazolo[5,4-d]-1,3-thiazole (B1): Beige crystalline product was obtained in the form of blocks, yield 70% (based on dithiooxamide), m.p. 240–244 °C. Elemental analysis (%): calcd C 52.54, H 2.20, N 10.21; found C 52.52, H 2.21, N 10.18.

FT-IR ATR: 3145(s), 3111(s), 3067(w), 2872(w), 2824(w), 2706(w), 2653(w), 2566(w), 2142(w), 1750(w), 1702(w), 1654(w), 1583(m), 1495(s), 1436(m), 1311(s), 1257(m), 1239(s), 1213(s), 1147(m), 1076(w), 1030(m), 1012(s), 926(m), 878(m), 844(s), 828(s), 752(m), 739(s), 660(m), 592(m) cm^{-1}.

NMR: ^{1}H NMR (400 MHz, DMSO-d_6): δ = 7.99 (m, 2H, **H$_c$**), 7.30 (m, 2H, **H$_a$**), 6.80 (m, 2H, **H$_b$**); ^{13}C{^{1}H} NMR (100 MHz, DMSO-d_6): δ = 158.3 (s, SCN, (**C2**)), 150.2 (s, **C**=**C** (**C1**)), 148.1 (s, OCC, (**C3**)) 146.2 (s, **C**-H$_c$ (**C6**)), 113.7 (s, **C**-H$_b$ (**C5**)), 111.6 (s, **C**-H$_a$ (**C4**)).

2,5-bis(2-thiophyl) -1,3-thiazolo[5,4-d]-1,3-thiazole (B2): The reaction mixture was heated at reflux in the microwave for 1 hour, after which it was allowed to cool down to room temperature. THF (ca. 5 mL) and chloranil (8.3 mmol) were added to the reaction mixture, which was refluxed for 10 minutes. The reaction was quenched by the addition of cold methanol (ca. 10 mL) and subsequent cooling to 0 °C. A yellow crystalline powder was obtained, yield 30% (based on dithiooxamide); m.p. 236–238 °C. Elemental analysis (%): calcd C 38.94, H 1.31, N 18.17; found C 38.90, H 1.29, N 18.19.

FTIR ATR: 3116(w), 3071(w), 1539(w), 1451(m), 1409(s), 1339(w), 1308(w), 1241(w), 1221(m), 1208(w), 1075(w), 1054(w), 969(s), 822(s), 707(s), 687(m), 614(w), 560(w), 483(w) cm^{-1}.

NMR: ^{1}H NMR (400 MHz, CDCl$_3$-d_1): δ = 7.58 (m, 2H, **H$_c$**), 7.46 (m, 2H, **H$_a$**), 7.12 (m, 2H, **H$_b$**); ^{13}C{^{1}H} NMR (100 MHz, CDCl$_3$-d_1): δ = 162.6 (s, SCN (**C2**)), 149.7 (s, **C**=**C** (**C1**)), 137.5 (s, SCC, (**C3**)), 128. 7 (s, **C**-H$_a$ (**C4**)), 128.1 (s, **C**-H$_b$ (**C5**)), 126.9 (s, **C**-H$_c$ (**C6**)).

2,5-bis(2-thiazolyl)-1,3-thiazolo[5,4-d]-1,3-thiazole (B3): The reaction mixture was heated at 120–125 °C for approximately 3 hours. A yellow crystalline product in the form of blocks was

obtained and purified in 30 mL of ethanol; yield 68.46% (based on dithiooxamide); m.p. 292.5–294.1 °C. Elemental analysis (%): calcd C 38.94, H 1.31, N 18.17; found C 38.90, H 1.29, N 18.19.

FTIR ATR: 3000(m), 3078(s), 3063(s), 1446(s), 1370(s), 1324(w), 1241(w), 1158(w), 1149(w), 1068(w), 1058(w), 980(s), 913(w), 845(s), 758(w), 742(s), 731(m), 698(w), 635(w), 615(w), 591(m), 499(w), 479(w) cm^{-1}.

NMR: ^{1}H NMR (400 MHz, CDCl$_3$-d_1): δ = 7.90 (d, $^3J_{HH}$ = 3, 2H, **H$_b$**), 7.48 (d, $^3J_{HH}$ = 3, 2H, **H$_a$**); ^{13}C{^{1}H} NMR (100 MHz, CDCl$_3$-d_1): δ = 171.15 (s, SCN, (**C2**)), 163.45 (s, SCN, (**C3′**)), 161.15 (s, SCN, (**C3**)),152. 11 (s, **C**=**C** (**C1**)), 144.33(s, **C**-H$_b$), 122.12 (s, **C**-H$_a$).

2,5-bis(2-imidazolyl)-1,3-thiazolo[5,4-d]-1,3-thiazole (B4): The reaction mixture was heated at 120–125 °C for approximately 3 hours. A brownish product in the form of crystalline powder was obtained; yield 75,44% (based on dithiooxamide); m.p. 323–338 °C. Elemental analysis (%): calcd C 43.48, H 2.20, N 30.64; found C 43.45, H 2.18, N 30.62. To obtain single crystals for XRD measurement, the compound was recrystallized from N,N-dimethylformamide.

FTIR ATR: 3123(w), 3059(w), 3013(m), 2925(m), 2860(m), 2806(m), 2766(m), 2713(s), 2680(s), 2590(m), 2535(m), 1653(w), 1484(m), 1448(m), 1431(w), 1363(s), 1297(m), 1157(w), 1118(s), 1050(w), 964(s), 926(w), 911(w), 870(m), 739(s), 710(m) cm^{-1}.

NMR: ^{1}H NMR (400 MHz, DMSO-d_6): δ = 13.43 (bs, 2H, **NH**), 7.43 (bs, 2H, **H$_a$**), 7.17 (bs, 2H, **H$_b$**); ^{13}C{^{1}H} NMR (100 MHz, DMSO-d_6): δ = 160.5 (s, SCN (**C2**)), 150.0 (s, **C** = **C** (**C1**)), 141.0 (s, NCNH (**C3**)), 131.0 (s, **C**H$_b$ (**C5**)), 121.0 (s, **C**H$_a$ (**C4**)).

2,5-bis((2E)-3-fenyloprop-2-enyl))-1,3-thiazolo[5,4-d]-1,3-thiazole (C): The reaction mixture was heated 130–140 °C for 3–3.5 hours. A light orange crystalline product was obtained; yield 70.53% (based on dithiooxamide); m.p. 239–242 °C. Elemental analysis (%): calcd C 69.33, H 4.07, N 8.09; found C 69.30, H 4.10, N 8.03.

FTIR ATR: 3103(w), 3080(w), 3052(w) 3032(m), 3011(w), 2993(m), 2805(w), 2635(w), 1947(w), 1875(w), 1779(w), 1745(w), 1698(w), 1662(w), 1624(m), 1595(w), 1576(w), 1497(m), 1453(w), 1427(s), 1332(w), 1301(w), 1254(m), 1220(s), 1187(s), 1172(s), 1100(w), 1071(m), 1029(w), 999(w), 973(w), 943(s), 847(s), 743(s), 682(s), 650(m), 603(w), 567(m), 491(m) cm^{-1}.

NMR: ^{1}H NMR (400 MHz, CDCl$_3$-d_1): δ = 7.58–7.54 (m, 4 H, *ortho*-C-**H** (**H$_o$**)), 7.50 (d, $^3J_{HH}$ = 16, 2 H, HC=CH, (**H$_a$**)), 7.44–7.35 (m, 6 H, *meta*- and *para*-C-**H**, (**H$_m$** and **H$_p$**)), 7.30 (d, $^3J_{HH}$=16, 2 H, HC=CH, (**H$_b$**)); ^{13}C{^{1}H} NMR (100 MHz, CDCl$_3$-d_1): δ = 168.2 (s, SCN (**C2**)), 150.3 (s, **C** = **C** (**C1**)), 135.4 (s, **C$_i$** (**C5**)), 135.1 (s, HC = CH (**C3**)), 129.4 (s, *meta*-**C**H (**C7** and **C9**)), 129.0 (s, *para*-**C**H (**C8**)), 127.3 (s, *ortho*-**C**H (**C6** and **C10**)), 122.12 (s, HC=CH (**C4**)).

Crystal structures: Crystal data, data collection, and structure refinement details are summarized in Table S1. The crystal structure data for **A3-A5, B1, and C**, were collected on an IPDS 2T dual beam diffractometer (STOE & Cie GmbH, Darmstadt, Germany) at 120.0(2) K with MoK$_\alpha$ radiation of a microfocus X-ray source — for **A4, A5, B1,** and **C** (GeniX 3D Mo High Flux, Xenocs, Sassenage, France) and CuK$_\alpha$ radiation for **A3**. A small crystal of **B4** was measured on Eulerian 4-circle diffractometer STOE Stadivari (Mo source, EIGER2 1 M CdTe detector). Crystals were cooled using a Cryostream 800 open-flow nitrogen cryostat (Oxford Cryosystems). The structures were solved using the intrinsic phasing procedure implemented in SHELXT and all nonhydrogen atoms were refined with anisotropic displacement parameters by the full-matrix least squares procedure based on F2 using the SHELX-2014 program package.[74] The Olex2[75] and Wingx[76] program suites were used to prepare the final version of CIF files. Olex2[76] and Mercury[77] were used to prepare the figures. Hydrogen atoms were refined using an isotropic model with U$_{iso}$(H) values fixed to be 1.2 or 1.5 times U$_{eq}$ of the carbon atoms

to which they were attached. Hydrogen atoms bonded to the electronegative oxygen or nitrogen atoms were located in the electron density maps and refined without constraints with the exception of **B4**.

DFT modelling: Single molecule calculations were performed using the Gaussian 16 Rev. C.01 software package[78] using the B3LYP hybrid functional[79] and a series of basis sets: 6–311 g,[80] CBSB7,[81] D95,[82] TZVP[83] and QZVP[83] basis sets under tight convergence criteria. It was found that the TZVP and QZVP basis sets give the lowest energies; however, the TZVP basis was found as a reasonable compromise between accuracy and computational cost. Results have been processed and visualized using the GaussView 5.08 software package.[84]

The geometry relaxation and the electronic structures (band structure and the density of states) calculations of the crystals were calculated using the plane-wave basis set and pseudopotentials implemented on the CASTEP (Cambridge Serial Total Energy Package) code. The PBE-GGA exchange-correlation function was applied, and the ion-electron interactions were defined using the projected augmented wave formalism. The noncovalent interaction corrections were applied in the calculation of DFT-MBD calculations. The periodic boundary conditions convergence tolerance such as cut-off energy, energy, maximum force, stress, and displacements were set to be 410 eV, 5×10^{-6} eV/atom, 0.01 eV/Å, 0.02 GPa, and 5×10^{-4} Å. A Monkhorst-Pack of k-points was applied to be $4 \times 3 \times 2$ for all the calculations. All the conditions were uniformly applied to all the crystal structures and molecules.

Spectroscopic measurements:

NMR spectroscopy: (^{1}H, ^{13}C{^{1}H}, ^{19}F) NMR spectra were recorded on a Bruker AV400 MHz spectrometer (external standard TMS for ^{1}H and ^{13}C and CFCl$_3$ for ^{19}F)) at ambient temperature. ^{1}H, ^{13}C{^{1}H}, and ^{19}F chemical shifts (δ) are reported in ppm relative to the residual solvent signals at 2.50 and 39.5 ppm (DMSO-d$_6$) and 7.26 and 77.16 ppm (CDCl$_3$-d$_1$). Coupling constants (J) are given in hertz (Hz). Multiplicities are abbreviated as singlet (s), doublet (d), triplet (t), quartet (q), multiplet (m), and broad (br). In order to improve the solubility of **B3** and enhance the peaks, a small amount of ethanol was added to the NMR tube.

FTIR ATR spectroscopy: FT-IR ATR spectra were recorded for the crystalline compounds using Nicolet iS50 equipped with a Specac Quest diamond ATR device; the spectra were collected and formatted by OMNIC software.

UV-Vis spectroscopy: Absorbance spectra for acetonitrile solution were measured on the Agilent 8453 UV-vis spectrometer in standard 1 cm quartz cells in the range 200 – 1200 nm with a resolution 1 nm.

Diffuse reflectance spectra for solid-state samples were measured on LAMBDA 750 UV/vis/NIR spectrophotometer equipped with a 100 mm integrating sphere (PerkinElmer Inc., USA). Spectra were recorded for powder samples prepared by grinding the mixture of powder samples with BaSO$_4$ in an agate mortar. BaSO$_4$ was used as a reference sample.

Photoluminescence spectra have been recorded on an FS5 (Edinburgh Instruments) spectrophotometer with high-pressure xenon lamp as the excitation source and a single-monochromator photomultiplier detector. The emission spectra were recorded in the range of 390–800 nm with a 375 nm excitation wavelength and a resolution of 1 nm. Measurements were conducted in standard 1 cm quartz cells for solutions or in solid-state sample holder for powder.

Time-resolved photoluminescence kinetic traces for all samples were recorded at room temperature using an FS5 spectrofluorometer (Edinburgh Instruments Company) in time-correlated single photon counting (TCSPC) mode. The EPL pulsed diode laser of 375 nm with a 50 ps pulse and repetition rate of 2 MHz (for solution) or 10 MHz (for powder) was used as the excitation source. The spectra were collected in a 20 ns time window with a time resolution of 2 ps. The instrument response function (IRF) has been recorded for light scattering ($\lambda_{ex} = \lambda_{em} = 375$ nm) independently for each sample.

The lifetime of fluorescence was determined by using Fluoracle software with the Reconvolution Fit Analysis function, including the IRF according to the fitting formula:

$$I(t) = B_1 \cdot e^{-\frac{t}{\tau_1}} + B_2 \cdot e^{-\frac{t}{\tau_2}} \tag{7}$$

where τ_1 - represents the lifetime of the radiative energy decay process, τ_2 - represents the lifetime of the nonradiative energy decay process, B_1, B_2 - fitting amplitudes corresponding to τ_1 and τ_2, respectively.

Synchrotron measurements - XAS at the S K-edge: Radial distribution functions were calculated for every S — S pair for the DFT-optimized.[85]

XAS was measured at the SOLARIS National Synchrotron Radiation of Poland.[86] The spectra at the S K-edge were collected at the bending magnet ASTRA beamline. A thin layer of powder samples was applied on a sulfur-free Kapton tape, and the excess was shaken off and removed with a cotton swab. The measurements were performed in transmission mode using an incident photon beam provided by a modified Lemonnier-type double-crystal monochromator equipped with InSb (111) crystals. For the monochromator energy calibration, we used a ZnSO$_4$ reference placed in the reference chamber, with a white line at 2481.4 eV. Positions of the absorption edges were determined based on a maximum of the first derivative of the spectrum. The final spectra were merged from at least three consecutive scans. All spectra were processed using the Athena program from the Demeter software package.[87]

XAS spectra were modeled using density functional theory (DFT) calculations performed with Finite Difference Method Near Edge Structure (FDMNES) software.[73] FDMNES is a user-friendly ab initio code that allows to simulating X-ray absorption and emission spectroscopies by solving the Schrödinger equation using local spin density approximation. The structure for the calculations was previously DFT-optimized using CASTEP. The finite difference method was used for X-ray absorption fine structure[88] with dipole ($\Delta l = \pm 1$) and 6 Å cluster radius. It was verified that the quadrupole transitions ($\Delta l = 0, \pm 2$) do not contribute to the spectrum; therefore, they were omitted. Relativistic and spin-orbit coupling effects were neglected. Lorentzian convoluted spectra were presented.

Electrical measurements: For thin film preparations, only representatives **A4, A5, B3, B4,** and **C** were chosen, based on their better solubility in DMF in comparison to the remaining compounds. Thin film samples were prepared according to the following procedural steps. Firstly, all compounds were dissolved in DMF (typically 50 mg of compound in 1 mL of DMF) and mixed on a magnetic stirrer at elevated temperatures (100 °C). Substrates, ITO glass (Ossila, The Netherlands), were washed (water, isopropyl alcohol), dried, and cleaned with O$_2$ plasma, then heated at 100 °C. Thin films were deposited on hot substrates via spincoating technique, typically 3000 rpm for 45 s and post-baked in 100 °C on a hotplate for 10 minutes. Copper electrodes were thermally deposited afterwards, through a shadow mask (Ossila, The Netherlands), with electrode dimensions of 1.3×1.5 mm.

All of the I-V responses, state retention measurements, endurance tests, and potentiation-depression tests were registered on an SP-300 potentiostat (BioLogic, France). Temperature-dependent I-V response measurements were conducted on the Instec TP102V Thermoelectric Probe Station. The system was designed as a two-terminal device, with the working electrode (WE) connected to Cu electrodes and the counter (CE) and reference (RE) electrodes were connected to the ITO substrate.

State-switching stability was evaluated for both the high-resistance state (HRS) and the low-resistance state (LRS). After applying a DC bias of either -3 V or $+3$ V for 1 s, the device state was measured at a reading voltage of $+500$ mV every 5 minutes over a period of 2 hours. The endurance test (on-off switching) was conducted by subjecting the devices to alternating extreme potential values (-3 V and $+3$ V) for 100 ms. This switching sequence was repeated 750 times, with the device state measured at a reading voltage of $+500$ mV after each cycle.

Acknowledgments

Conflict of Interests

The authors declare no conflict of interest.

Data Availability Statement

The data that support the findings of this study are available in the supplementary material of this article.

[1] (a) A. Khasbaatar, Z. Xu, J.-H. Lee, G. Campillo-Alvarado, C. Hwang, B. N. Onusaitis, Y. Diao, *Chem. Rev.* **2023**, *123*, 8395; (b) L. Ding, Z.-D. Yu, X.-Y. Wang, Z.-F. Yao, Y. Lu, C.-Y. Yang, J.-Y. Wang, J. Pei, *Chem. Rev.* **2023**, *123*, 7421; (c) G. Zhang, F. R. Lin, F. Qi, T. Heumüller, A. Distler, H.-J. Egelhaaf,

N. Li, P. C. Y. Chow, C. J. Brabec, A. K. Y. Jen, H.-L. Yip, *Chem. Rev.* **2022**, *122*, 14180.

[2] (a) F. Yang, S. Cheng, X. Zhang, X. Ren, R. Li, H. Dong, W. Hu, *Adv. Mater.* **2018**, *30*, 1702415; (b) A. Mahmood, *J. Cluster Sci.* **2019**, *30*, 1123; (c) M. Khalid, A. Ali, M. Adeel, Z. U. Din, M. N. Tahir, E. Rodrigues-Filho, J. Iqbal, M. U. Khan, *J. Mol. Struct.* **2020**, *1206*, 127755; (d) N. A. Kukhta, M. R. Bryce, *Mater. Horiz.* **2021**, *8*, 33; (e) F. Gao, E. Reichmanis, *Chem. Rev.* **2023**, *123*, 10835; (f) J. W. Lim, in *Materials* **2024**, *17*,.

[3] (a) H. Yao, J. Wang, Y. Xu, S. Zhang, J. Hou, *Acc. Chem. Res.* **2020**, *53*, 822; (b) D. Meng, R. Zheng, Y. Zhao, E. Zhang, L. Dou, Y. Yang, *Adv. Mater.* **2022**, *34*, 2107330; (c) B. Fan, F. Lin, X. Wu, Z. Zhu, A. K. Y. Jen, *Acc. Chem. Res.* **2021**, *54*, 3906; (d) M. D. M. Faure, B. H. Lessard, *J. Mater. Chem. C* **2021**, *9*, 14; (e) E. K. Solak, E. Irmak, *RSC Adv.* **2023**, *13*, 12244.

[4] (a) A. Calabrese, P. Battistoni, S. Ceylan, L. Zeni, A. Capo, A. Varriale, S. D'Auria, M. Staiano, in *Biosensors* **2023**, *13*; (b) D. Deng, Y. Chang, W. Liu, M. Ren, N. Xia, Y. Hao, in *Biosensors* **2023**, *13*; (c) J. B. Kaushal, P. Raut, S. Kumar, in *Biosensors* **2023**, *13*; (d) J. Ma, T. Shu, Y. Sun, X. Zhou, C. Ren, L. Su, X. Zhang, *Small* **2022**, *18*, 2103516; (e) C. Sun, X. Wang, M. A. Auwalu, S. Cheng, W. Hu, *EcoMat* **2021**, *3*, e12094.

[5] (a) R. Iftikhar, F. Z. Khan, N. Naeem, *Mol. Diversity* **2024**, *28*, 271; (b) R. J. Pandhare, P. M. Badani, R. M. Kamble, *J. Mol. Struct.* **2024**, *1298*, 137080; (c) K. Upendranath, T. Venkatesh, T. N. Lohith, M. A. Sridhar, *J. Mol. Struct.* **2022**, *1264*, 133231; (d) J. V. Vaghasiya, C. C. Mayorga-Martinez, M. Pumera, *Chem. Soc. Rev.* **2020**, *49*, 7819; (e) Y. Zhang, J. Song, J. Qu, P.-C. Qian, W.-Y. Wong, *Sci. China: Chem.* **2021**, *64*, 341.

[6] (a) D. Bevk, L. Marin, L. Lutsen, D. Vanderzande, W. Maes, *RSC Adv.* **2013**, *3*, 11418; (b) P. Maienfisch, A. J. F. Edmunds, in *Advances in Heterocyclic Chemistry*, *Vol. 121*, (Eds.: E. F. V. Scriven, C. A. Ramsden), Academic Press, **2017**, pp. 35; (c) M. Saito, I. Osaka, Y. Suzuki, K. Takimiya, T. Okabe, S. Ikeda, T. Asano, *Sci. Rep.* **2015**, *5*, 14202; (d) P. Zahradník, P. Magdolen, P. Zahradník, *Tetrahedron Lett.* **2010**, *51*, 5819.

[7] J. Y. Jung, S. J. Han, J. Chun, C. Lee, J. Yoon, *Dyes Pigm.* **2012**, *94*, 423.

[8] (a) J. R. Johnson, R. Ketcham, *J. Am. Chem. Soc.* **1960**, *82*, 2719; (b) J. R. Johnson, D. H. Rotenberg, R. Ketcham, *J. Am. Chem. Soc.* **1970**, *92*, 4046.

[9] R. Ketcham, S. Mah, *J. Med. Chem.* **1971**, *14*, 743.

[10] X. Huang, W. Lu, Q. Liu, M. Wu, *Comput Theor Chem* **2023**, *1230*, 114387.

[11] (a) A. Shibu, S. Jones, P. L. Tolley, D. Diaz, C. O. Kwiatkowski, D. S. Jones, J. M. Shivas, J. J. Foley, T. A. Schmedake, M. G. Walter, *Mater. Adv.* **2023**, *4*, 6321; (b) A. Thorat, S. Behera, A. A. Boopathi, C. Kulkarni, *Angew. Chem., Int. Ed.* **2024**, *63*, e202409725; (c) W. Zhou, D. Wu, H. Xiao, J. Song, L. Qu, L. Wang, X. Zhou, Z.-X. Xu, H. Xiang, *Dyes Pigm* **2022**, *197*, 109906.

[12] (a) A. R. Brotherton, A. Shibu, J. C. Meadows, N. A. Sayresmith, C. E. Brown, A. M. Ledezma, T. A. Schmedake, M. G. Walter, *Adv. Sci.* **2023**, *10*, 2205729; (b) Y. Liu, Z. Liang, Z. Li, K. Zhao, Y. Sun, X. Zhang, R. Yang, L. Qu, *Microchem. J.* **2020**, *154*, 104640; (c) S. Shah, N. Naithani, S. C. Sahoo, P. P. Neelakandan, N. Tyagi, *J. Mater. Chem. C* **2024**, *12*, 13088.

[13] (a) A. F. R. Cerqueira, M. E. Pérez, N. S. Gsponer, M. G. P. M. S. Neves, A. Jorge Parola, E. N. Durantini, A. C. Tomé, *J. Photochem Photobiol A* **2024**, *456*, 115849; (b) A. F. R. Cerqueira, N. M. M. Moura, M. G. P. M. S. Neves, A. Jorge Parola, A. C. Tomé, *J. Photochem Photobiol A* **2024**, *451*, 115490; (c) V. Kumar, S. Sony, N. Kaur, S. M. Mobin, P. Kaur, K. Singh, *Anal. Chim. Acta* **2022**, *1206*, 339776.

[14] X. Li, C. Huang, Y. Fan, Z. Bai, B.-L. An, J. Xu, W. Zheng, Y.-L. Bai, *ACS Appl. Mater. Interfaces* **2023**, *15*, 46022.

[15] (a) R. Li, X. Yang, *J. of Physica Chemistry A* **2019**, *123*, 10102; (b) A. N. Woodward, J. M. Kolesar, S. R. Hall, N.-A. Saleh, D. S. Jones, M. G. Walter, *J. Am. Chem. Soc.* **2017**, *139*, 8467.

[16] M. Samal, S. Valligatla, N. A. Saad, M. V. Rao, D. N. Rao, R. Sahu, B. P. Biswal, *Chem. Commun.* **2019**, *55*, 11025.

[17] H. M. Tay, C. Hua, *CrystEngComm* **2020**, *22*, 6690.

[18] (a) S. Ando, J.-i. Nishida, Y. Inoue, S. Tokito, Y. Yamashita, *J. Mater. Chem.* **2004**, *14*, 1787; (b) S. Van Mierloo, S. Chambon, A. E. Boyukbayram, P. Adriaensens, L. Lutsen, T. J. Cleij, D. Vanderzande, *Magn. Reson. Chem.* **2010**, *48*, 362; (c) S. Ando, J. Nishida, E. Fujiwara, H. Tada, Y. Inoue, S. Tokito, Y. Yamashita, *Synth. Met.* **2006**, *156*, 327; (d) J.-M. Jiang, M.-C. Yuan, K. Dinakaran, A. Hariharan, K.-H. Wei, *J. Mater. Chem. A* **2013**, *1*, 4415; (e) I. Osaka, G. Sauvé, R. Zhang, T. Kowalewski, R. D. McCullough, *Adv. Mater.* **2007**, *19*, 4160; (f) A. Datta, P. Pal, R. Mondal, S. Malik, *Polym. Chem.* **2024**, *15*, 4699.

[19] (a) T. Naito, Y. Kita, T. Shimazaki, M. Tachikawa, *RSC Adv.* **2022**, *12*, 34685; (b) V. Malytskyi, J.-J. Simon, L. Patrone, J.-M. Raimundo, *RSC Adv.* **2015**,

Chem. Eur. J. **2025**, *0*, e202501664 (22 of 24)

© 2025 The Author(s). Chemistry – A European Journal published by Wiley-VCH GmbH

Chemistry–A European Journal

Research Article

doi.org/10.1002/chem.202501664

Chemistry Europe

European Chemical
Societies Publishing

5, 354; (c) A. Dessì, M. Calamante, A. Mordini, M. Peruzzini, A. Sinicropi, R. Basosi, F. Fabrizi de Biani, M. Taddei, D. Colonna, A. Di Carlo, G. Reginato, L. Zani, *Chem. Commun.* **2014**, *50*, 13952; (d) T. Shimazaki, M. Tachikawa, *Phys. Chem. Chem. Phys.* **2021**, *23*, 21078.

[20] M. Mamada, J.-i. Nishida, D. Kumaki, S. Tokito, Y. Yamashita, *Chem. Mater.* **2007**, *19*, 5404.

[21] Z. Zhang, Y.-A. Chen, W.-Y. Hung, W.-F. Tang, Y.-H. Hsu, C.-L. Chen, F.-Y. Meng, P.-T. Chou, *Chem. Mater.* **2016**, *28*, 8815.

[22] C. Singh, N. Ray, in *Optical Properties of Metal Oxide Nanostructures* (Eds.: V. Kumar, I. Ayoub, V. Sharma, H. C. Swart), Springer Nature Singapore, Singapore, **2023**, pp. 431.

[23] (a) K. C. Kwon, J. H. Baek, K. Hong, S. Y. Kim, H. W. Jang, *Nano-Micro Lett.* **2022**, *14*, 58; (b) W. Huh, D. Lee, C.-H. Lee, *Adv. Mater.* **2020**, *32*, 2002092.

[24] S. Satapathi, K. Raj, Yukta, M. A. A., *Phys. Rev. Appl.* **2022**, *18*, 017001.

[25] Y. Feng, X. Qiao, G. Ouyang, G. Liu, H. Li, *Adv. Electron. Mater.* **2020**, *6*, 1901443.

[26] S. L. Nikitenko, P. I. Proshin, I. E. Kuznetsov, S. V. Karpov, D. V. Anokhin, D. A. Ivanov, P. A. Troshin, A. V. Akkuratov, *Sol. Energy* **2022**, *232*, 12.

[27] Q. Zhang, D. Wu, Y. Fu, J. Li, Y. Chen, B. Zhang, *ACS Appl. Mater. Interfaces* **2024**, *16*, 22217.

[28] A. Sławek, L. Alluhaibi, E. Kowalewska, G. Abdi, T. Mazur, A. Podborska, K. Mech, M. Marciszko-Wiąckowska, A. Maximenko, K. Szaciłowski, *Adv. Electron. Mater.* **2024**, 2300818.

[29] A. Hantzsch, *Ber. Dtsch. Chem. Ges.* **1881**, *14*, 1637.

[30] J. Ephraim, *Ber. Dtsch. Chem. Ges.* **1891**, *24*, 1026.

[31] (a) K. Wang, H. Zhang, S. Chen, G. Yang, J. Zhang, W. Tian, Z. Su, Y. Wang, *Adv. Mater.* **2014**, *26*, 6168; (b) M. Ghora, P. Majumdar, M. Anas, S. Varghese, *Chem. Eur. J.* **2020**, *26*, 14488.

[32] A. Bolognesi, M. Catellani, S. Destri, W. Porzio, *Acta Crystallogr. C* **1987**, *43*, 2106.

[33] J. E. Campbell, J. Yang, G. M. Day, *J. Mater. Chem. C* **2017**, *5*, 7574.

[34] L. D. Costa, S. Guieu, M. d. A. F. Faustino, A. C. Tomé, *New J. Chem.* **2022**, *46*, 3602.

[35] D. Li, Z. Zhang, S. Zhao, Y. Wang, H. Zhang, *Dalton Trans.* **2011**, *40*, 1279.

[36] B. P. Biswal, D. Becker, N. Chandrasekhar, J. S. Seenath, S. Paasch, S. Machill, F. Hennersdorf, E. Brunner, J. J. Weigand, R. Berger, X. Feng, *Chem. Eur. J.* **2018**, *24*, 10868.

[37] S. Ando, J.-i. Nishida, H. Tada, Y. Inoue, S. Tokito, Y. Yamashita, *J. Am. Chem. Soc.* **2005**, *127*, 5336.

[38] P. Wagner, M. Kubicki, *Acta Crystallogr. C* **2003**, *59*, o91-o92.

[39] T. Tao, J. Geng, L. Hong, W. Huang, H. Tanaka, D. Tanaka, T. Ogawa, *J. Phys. Chem. C* **2013**, *117*, 25325.

[40] R. J. Baker, P. E. Colavita, D. M. Murphy, J. A. Platts, J. D. Wallis, *J. Phys. Chem. A* **2012**, *116*, 1435.

[41] P. R. Spackman, M. J. Turner, J. J. McKinnon, S. K. Wolff, D. J. Grimwood, D. Jayatilaka, M. A. Spackman, *J. Appl. Crystallogr.* **2021**, *54*, 1006.

[42] (a) X. Yu, L. Zheng, J. Li, P. Yu, Z. Liu, C. Li, Y. Zou, X. Zhang, W. Hu, *Org. Electron.* **2020**, *87*, 105941; (b) J.-I. Park, J. W. Chung, J.-Y. Kim, J. Lee, J. Y. Jung, B. Koo, B.-L. Lee, S. W. Lee, Y. W. Jin, S. Y. Lee, *J. Am. Chem. Soc.* **2015**, *137*, 12175; (c) J. Podlesný, F. Bureš, in *Organics* **2022**, *3*, pp. 446.

[43] (a) Y. A. Berlin, G. R. Hutchison, P. Rempala, M. A. Ratner, J. Michl, *J. Phys. Chem. A* **2003**, *107*, 3970; (b) S. T. Bromley, M. Mas-Torrent, P. Hadley, C. Rovira, *J. Am. Chem. Soc.* **2004**, *126*, 6544; (c) R. A. Marcus, *Rev. Mod. Phys.* **1993**, *65*, 599; (d) R. A. Marcus, *J. Chem. Phys.* **2004**, *26*, 867; (e) R. A. Marcus, *J. Chem. Phys.* **2004**, *26*, 872; (f) R. A. Marcus, *J. Chem. Phys.* **2004**, *24*, 966.

[44] (a) O. López-Estrada, H. G. Laguna, C. Barrueta-Flores, C. Amador-Bedolla, *ACS Omega* **2018**, *3*, 2130; (b) P. K. Behara, M. Dupuis, *Phys. Chem. Chem. Phys.* **2020**, *22*, 10609.

[45] A. Datta, S. Mohakud, S. K. Pati, *J. Mater. Chem.* **2007**, *17*, 1933.

[46] E. Cechosz, L. Alluhaibi, T. Mazur, A. Sławek, N. Pandurangan, K. Szaciłowski, *Adv. Electron. Mater.* **2024**, *n/a*, 2400654.

[47] S. Slassi, M. Aarjane, A. Amine, *J. Mol. Struct.* **2023**, *1276*, 134788.

[48] (a) V. S. Naik, P. S. Patil, Q. A. Wong, C. K. Quah, N. B. Gummagol, H. S. Jayanna, *J. Mol. Struct.* **2020**, *1222*, 128901; (b) V. S. Naik, A. Pragasam, H. S. Jayanna, G. Vinitha, *Chem. Phys. Lett.* **2020**, *754*, 137680.

[49] (a) K. Pyta, P. Przybylski, A. Huczyński, A. Hoser, K. Woźniak, W. Schilf, B. Kamieński, E. Grech, B. Brzezinski, *J. Mol. Struct.* **2010**, *970*, 147; (b) A. Mielcarek, A. Wiśniewska, A. Dołęga, *Struct. Chem.* **2018**, *29*, 1189.

[50] (a) P. Rajkumar, S. Selvaraj, P. Anthoniammal, A. Ram Kumar, K. Kasthuri, S. Kumaresan, *Chem Phys Impact* **2023**, *7*, 100257; (b) R. P. C. L. Sousa, R.

B. Figueira, B. R. Gomes, S. Sousa, R. C. M. Ferreira, S. P. G. Costa, M. M. M. Raposo, in *Nanomaterials* **2021**, *11*,.

[51] B. Brzezinski, G. Zundel, *J. Phys. Chem.* **1982**, *86*, 5133.

[52] M. Ventura, J. R. Silva, T. Catunda, L. H. C. Andrade, S. M. Lima, *J. Mol. Liq.* **2021**, *328*, 115414.

[53] (a) O. Unsalan, H. Arı, C. Altunayar-Unsalan, K. Bolelli, M. Boyukata, I. Yalcin, *J. Mol. Struct.* **2020**, *1218*, 128454; (b) T.-X. Luan, P. Zhang, Q. Wang, X. Xiao, Y. Feng, Y. Suan, P.-Z. Li, Q. Xu, *Nano Lett.* **2024**, *24*, 5075.

[54] (a) P. Sowmya, S. Prakash, A. Joseph, *J. Solid State Chem.* **2023**, *320*, 123836; (b) R. Balogh, A. Eckstein, K. Tokár, M. Danko, *J. Photochem. Photobiol., A* **2023**, *434*, 114217; (c) X. Lv, Q. Hu, T. Miao, Y. Li, B. Cui, Y. Fang, *Anal. Bioanal. Chem.* **2022**, *414*, 4837.

[55] U. Olgun, Z. Dikmen, H. Çetin, F. Arıcan, M. Gülfen, *J. Mol. Struct.* **2022**, *1250*, 131816.

[56] (a) A. Rocheteau, L. Lemeur, M. Cordier, M. Paris, J.-Y. Mevellec, C. Latouche, H. Serier-Brault, S. Perruchas, *Adv.Opt. Mater.* **2024**, *n/a*, 2402040; (b) B. Liu, Q. Zhou, Y. Li, Y. Chen, D. He, D. Ma, X. Han, R. Li, K. Yang, Y. Yang, S. Lu, X. Ren, Z. Zhang, L. Ding, J. Feng, J. Yi, J. Chen, *Angew. Chem., Int. Ed.* **2024**, *63*, e202317185; (c) T. G. Paiva, M. Klem, S. L. Silvestre, J. Coelho, N. Alves, E. Fortunato, E. J. Cabrita, M. C. Corvo, *ChemSusChem* **2024**, *n/a*, e202401710; (d) R. A. Yadav, M. Kumar, R. Singh, P. Singh, S. Jaiswal, G. Srivastav, R. L. Prasad, *Spectrochim. Acta, Part A* **2008**, *71*, 1565.

[57] R. Berger, G. Resnati, P. Metrangolo, E. Weber, J. Hulliger, *Chem. Soc. Rev.* **2011**, *40*, 3496.

[58] M. Asemani, A. R. Rabbani, *J. Pet Sci Eng* **2020**, *185*, 106618.

[59] X. Li, Y. Ju, Q. Hou, H. Lin, *Sci China Earth Sci* **2012**, *55*, 1269.

[60] A. K. Sahoo, C. Yadav, J. N. Moorthy, *Appl. Catal. A Gen.* **2024**, *671*, 119557.

[61] (a) M. D. Smith, B. L. Watson, R. H. Dauskardt, H. I. Karunadasa, *Chem. Mater.* **2017**, *29*, 7083; (b) C. H. Cheng, H. Y. Huang, M. J. Talite, W. C. Chou, J. M. Yeh, C. T. Yuan, *J. Colloid Interface Sci.* **2017**, *508*, 105.

[62] (a) S. Kumar, M. Singh, P. Gaur, J.-H. Jou, S. Ghosh, *ACS Omega* **2017**, *2*, 5348; (b) H. Wu, S. Wang, J. Ding, R. Wang, Y. Zhang, *Dyes Pigm* **2020**, *182*, 108665.

[63] S. J. Cassidy, I. Brettell-Adams, L. E. McNamara, M. F. Smith, M. Bautista, H. Cao, M. Vasiliu, D. L. Gerlach, F. Qu, N. I. Hammer, D. A. Dixon, P. A. Rupar, *Organometallics* **2018**, *37*, 3732.

[64] (a) E. Lippert, **1955**, *10*, 541; (b) N. Mataga, Y. Kaifu, M. Koizumi, *Bull. Chem. Soc. Jpn.* **1955**, *28*, 690.

[65] (a) M. R. Pinto, Y. Takahata, T. D. Z. Atvars, *J. Photochem. Photobiol., A* **2001**, *143*, 119; (b) A. Brillante, B. Samorì, C. Stremmenos, P. Zanirato, *Mol. Cryst. Liq. Cryst.* **1983**, *100*, 263.

[66] S. Landi, I. R. Segundo, E. Freitas, M. Vasilevskiy, J. Carneiro, C. J. Tavares, *Solid State Commun.* **2022**, *341*, 114573.

[67] J. I. Pankove, *Optical Processes in Semiconductors*, Dover Publications, Inc., Mineola NY, **1975**.

[68] J. Tauc, in *Amorphous and Liquid Semiconductors* (Ed.: J. Tauc), Plenum Press, London, **1974**.

[69] (a) S. Kasap, C. Koughia, J. Singh, H. Ruda, S. O'Leary, in *Springer Handbook ofElectronic and PhotonicMaterials* (Eds.: S. Kasap, P. Capper), Springer US, Boston, MA, **2007**, pp. 47; (b) K. Morigaki, C. Ogihara, in *Springer Handbook of Electronic and Photonic Materials* (Eds.: S. Kasap, P. Capper), Springer US, Boston, MA, **2007**, pp. 565.

[70] E. I. Solomon, B. Hedman, K. O. Hodgson, A. Dey, R. K. Szilagyi, *Coord. Chem. Rev.* **2005**, *249*, 97.

[71] G. Almkvist, K. Boye, I. Persson, *J. Synchrotron Radiat.* **2010**, *17*, 683.

[72] (a) R. A. Mori, E. Paris, G. Giuli, S. G. Eeckhout, M. Kavčič, M. Žitnik, K. Bučar, L. G. M. Pettersson, P. Glatzel, *Anal. Chem.* **2009**, *81*, 6516; (b) G. Almkvist, K. Boye, I. Persson, *J. Synchrotron Radiat.* **2010**, *17*, 683.

[73] O. Bunău, Y. Joly, *J. Phys.: Condens. Matter* **2009**, *21*, 345501.

[74] G. Sheldrick, *Acta Cryst. C* **2015**, *71*, 3.

[75] O. V. Dolomanov, L. J. Bourhis, R. J. Gildea, J. A. K. Howard, H. Puschmann, *J. Appl. Crystallogr.* **2009**, *42*, 339.

[76] L. Farrugia, *J. Appl. Crystallogr.* **2012**, *45*, 849.

[77] C. F. Macrae, P. R. Edgington, P. McCabe, E. Pidcock, G. P. Shields, R. Taylor, M. Towler, J. van de Streek, *J. Appl. Crystallogr.* **2006**, *39*, 453.

[78] M. J. Frisch, G. W. Trucks, H. B. Schlegel, G. E. Scuseria, M. A. Robb, J. R. Cheeseman, G. Scalmani, V. Barone, G. A. Petersson, H. Nakatsuji, X. Li, M. Caricato, A. V. Marenich, J. Bloino, B. G. Janesko, R. Gomperts, B. Mennucci, H. P. Hratchian, J. V. Ortiz, A. F. Izmaylov, J. L. Sonnenberg,

Chemistry–A European Journal

Research Article
doi.org/10.1002/chem.202501664

Chemistry Europe
European Chemical
Societies Publishing

Williams F. D., F. Lipparini, F. Egidi, J. Goings, B. Peng, A. Petrone, T. Henderson, D. Ranasinghe, V. G. Zakrzewski et al., *Gaussian 16, Rev. C.01*, Gaussian, Inc., Wallingford CT, **2019**.

[79] A. D. Becke, *J. Chem. Phys.* **1993**, *98*, 5648.

[80] (a) A. D. McLean, G. S. Chandler, *J. Chem. Phys.* **1980**, *72*, 5639; (b) R. Krishnan, J. S. Binkley, R. Seeger, J. A. Pople, *J. Chem. Phys.* **1980**, *72*, 650.

[81] J. A. Montgomery, Jr., M. J. Frisch, J. W. Ochterski, G. A. Petersson, *J. Chem. Phys.* **1999**, *110*, 2822.

[82] T. H. D. Jr,, P. J. Hay, *Modern Theoretical Chemistry*, Plenum Press, New York, **1977**.

[83] N. M. Weinberger, *Sci. Am.* **2004**, *291* 88.

[84] R. T. Dennington, T. Keith, J. Millam, Semichem Inc. Shawnee Mission KS, **2009**.

[85] A. Stukowski, *Sci Eng* **2010**, *18*, 015012.

[86] J. Szlachetko, J. Szade, E. Beyer, W. Błachucki, P. Ciochoń, P. Dumas, K. Freindl, G. Gazdowicz, S. Glatt, K. Guła, J. Hormes, P. Indyka, A. Klonecka, J. Kołodziej, T. Kołodziej, J. Korecki, P. Korecki, F. Kosiorowski, K. Kosowska, G. Kowalski, M. Kozak, P. Kozioł, W. Kwiatek, D. Liberda, H. Lichtenberg, E. Madej, A. Mandziak, A. Marendziak, K. Matlak, A. Maximenkoet al., *Eur. Phys. J. Plus* **2023**, *138*, 10.

[87] B. Ravel, M. Newville, *J. Synchrotron Radiat.* **2005**, *12*, 537.

[88] J. D. Bourke, C. T. Chantler, Y. Joly, *J. Synchrotron Radiat.* **2016**, *23*, 551.

RESEARCH ARTICLE

TzTz derivatives are promising materials for flexible optoelectronic and sensing applications due to their easy synthesis, tunable properties, and stability. This study analyzes 10 TzTz derivatives, detailing their synthesis, spectroscopic characterization (FTIR, NMR, UV-Vis), fluorescence behavior, and synchrotron XANES findings, showcasing their potential for advanced electronic and optoelectronic devices.
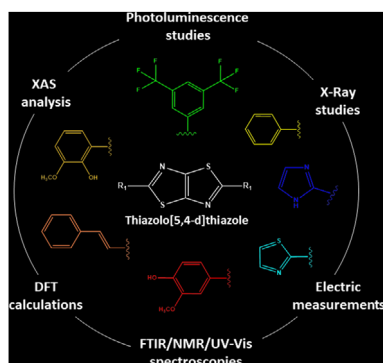
K. Gutmańska, A. Podborska, A. Sławek, R. Sivasamy, L. Alluhaibi, A. Maximenko, A. Ordyszewska, K. Szaciłowski, A. Dołęga, T. Mazur

1 – 24

Structural Insights and Advanced Spectroscopic Characterization of Thiazolothiazoles: Unveiling Potential for Optoelectronic and Sensing Applications